Finite Element Modeling and experimental validation of Concentrator Photovoltaic module based on Surface Mount Technology

Konan Kouame, D. Danovitch, P. Albert, A. Turala, M. Volatier, V. Aimez, A. Jaouad, Maxime Darnon, G. Hamon

Finite Element Modeling and experimental validation of Concentrator Photovoltaic module based on Surface Mount Technology

Konan Kouame[1,2], D. Danovitch[1,2], P. Albert[1,2], A. Turala[1,2], M. Volatier[1,2], V. Aimez[1,2], A. Jaouad[1,2], M. Darnon[1,2], G. Hamon[1,2]

[1] Laboratoire Nanotechnologies Nanosystèmes (LN2) - CNRS IRL-3463 Institut Interdisciplinaire d′Innovation Technologique (3IT), Université de Sherbrooke, 3000 Boulevard Université, Sherbrooke, J1K 0A5 Québec, Canada

[2] Institut Interdisciplinaire d′Innovation Technologique (3IT), Université de Sherbrooke, 3000 Boulevard Université, Sherbrooke, J1K 0A5, QC, Canada

konan.jean.herbert.kouame@usherbrooke.ca

***Abstract* — The development of renewable and clean energy such as concentrator photovoltaics (CPV) has been spurred by the scarcity of fossil fuels and their impact on global warming. However, CPV is expensive and complex to assemble, which has led to the creation of a new assembly method based on Surface Mount Technologies (SMT). In this study, we used Finite Element Model (FEM) to investigate and optimize thermal performance of such an assembly. We first fabricated and characterized a 4-solar cell CPV SMT module to enable comparison between experimental and FEM predicted temperatures. Following this validation, a parametric study was conducted. The model was extended to an infinite number of solar cells to guide the design of a large-scale SMT-based CPV module. The optimal dimensions were determined by identifying the module parameters that affect cell temperature, such as the area and thickness of the metal ribbon on the backside of the solar cell and metal coverage on the transparent glass Printed Circuit Board (PCB) on the frontside of the solar cell. Furthermore, the results of the parametric simulation have confirmed our previous findings, indicating that the module assembled using the simplified SMT method, with optimal dimensions of the metal ribbon, exhibits superior heat dissipation compared to the standard design based on wire bonding, due to the presence of metal on the glass printed circuit board. Further, this work demonstrates that by optimizing the SMT design with FEM, the temperature of the solar cells can be maintained below 80°C.**

Keywords – photovoltaics, concentrator photovoltaic, CPV, surface mount technologies, SMT, thermal simulation, finite elements modeling, FEM, solar cell assembly

I. Introduction

The increasing scarcity and price of fossil fuels and their impact on global warming have spurred the development of new forms of clean, renewable energy, such as concentrator photovoltaics (CPV). This technology increases the energy efficiency of photovoltaic systems and has achieved a record efficiency of 47.6% at a concentration of 665× [1]. The majority of commercial CPV modules use FLATCON (Frensel Lens All glass Tandem cell CONcentrator module) technology [2], [3], [4], [5]. However, other CPV technologies use mirrors instead of lenses to concentrate light on solar cells or onto a Dense Receiver Array (DRA) [6]. In FLATCON modules, the solar cells are placed by pick and place and connected by wire bonding. Pick and place and wire bonding can lead to solar cell placement errors and long assembly times respectively, especially for sub-millimeter microcells [7]. Placement errors and long assembly times result in poor module performance [7] and low production output, respectively. To improve alignment accuracy and reduce microcell assembly time, various methods have been developed. Semprius transfer printing [8] aims to simultaneously place several solar cells from a source wafer onto a receiver substrate using a buffer, but this method is not suitable for high-volume applications due to its high-precision pick-and-place equipment requirements and the use of wire bonding. Panasonic used fluidic self-assembly [7] and SMT (Surface Mount Technology) [9] approaches to reduce assembly time and improve alignment accuracy. Fluidic self-assembly offers alignment accuracy comparable to

that of the SMT but takes longer to assemble. The SMT, which uses a conductive solder paste for interconnection, has the advantage of being less expensive [10], faster for large-scale production [11], and SMT equipment takes up less space than wire-based wiring equipment [10].

In our published work [12], we have developed and employed the SMT process, which integrates assembly flexibility and enhanced alignment of solar cells, to assembly the solar cells larger than a millimeter in size.

Since a new assembly method (SMT) is used, efficient heat dissipation is essential to avoid early degradation and/or performance deterioration of the solar cell. Cell suppliers recommend an operating temperature of 100°C-120°C [13], [14], [15], but research [16] proposes a temperature of 80°C to avoid rapid degradation of solar cell in CPV module. Indeed, P. Espinet-González et al. [16] carried out an accelerated ageing study of solar cells, examining two nominal operating conditions at temperatures of 80 and 100°C. In both cases, the instantaneous failure rate increased monotonically, indicating wear-type failures. The results highlight the high sensitivity of the reliability data to the nominal temperature. For example, for nominal operating conditions at 820 suns at 80°C, with daily use of 5 hours, the warranty period was 113 years for a 5% failure. However, for similar conditions at 100°C, the warranty period for a 5%

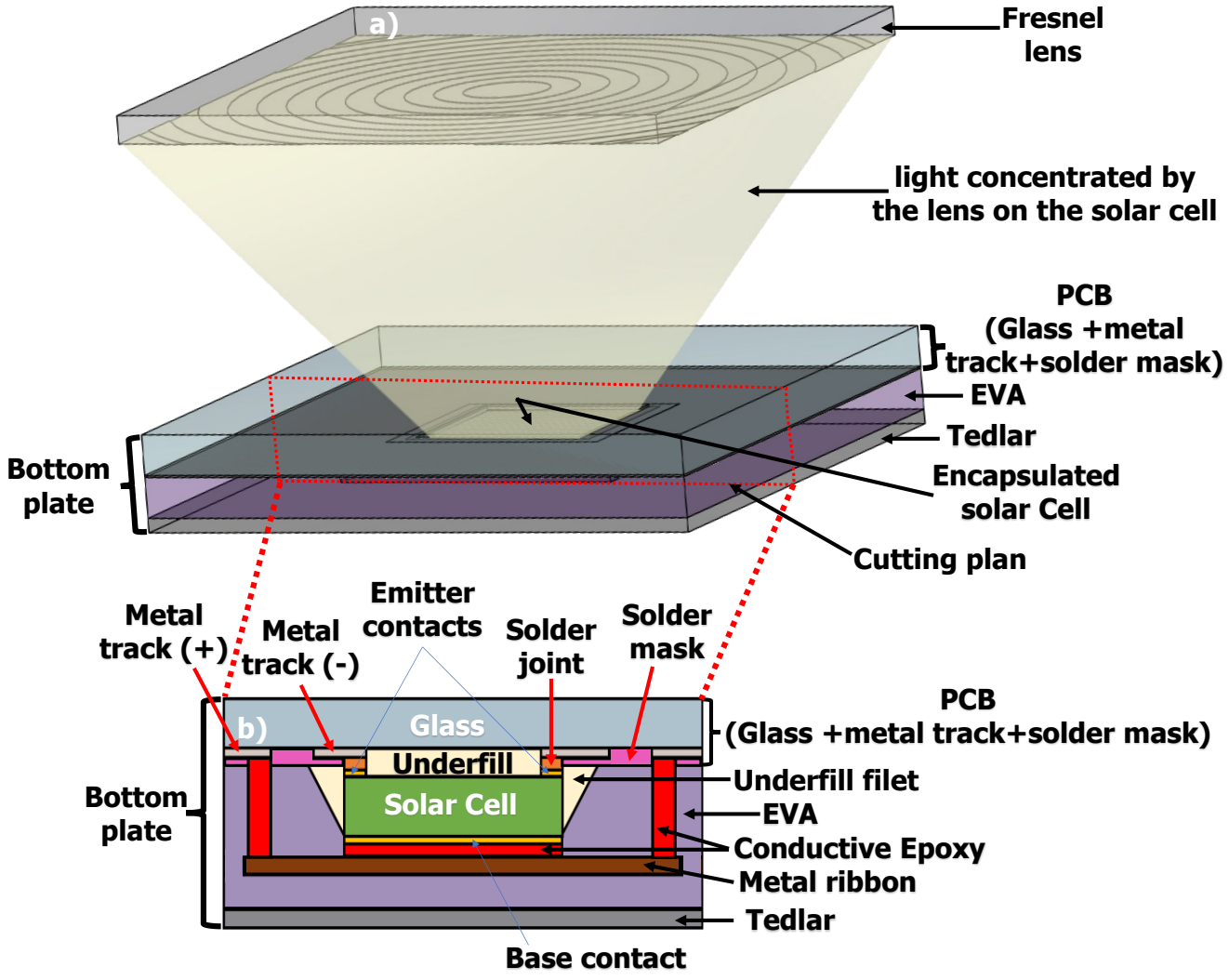

Fig. 1. a) 3D figure illustrating the concentration of light by the lens on the solar cell encapsulated in the Bottom plate, b) cross-section of the Bottom plate.

failure was reduced to 7 years. The assessment of temperature impact on solar cell performance relies on the use of temperature coefficients. Various publications address this measure in diverse ways. In reference [17], the temperature coefficient is determined by calculating the variation of open-circuit voltage with respect to temperature. Another approach to express this coefficient is presented in reference [13], where it is depicted as the variation of efficiency with temperature. For instance, for an Azur Space III-V solar cell, the temperature coefficient is established as $\Delta\eta/\Delta T$ = -0.046% Abs/K [13].

The ability of a package to dissipate heat depends on the geometry and thermal properties of its materials. Finite Element Modeling (FEM) is a method used to represent three-dimensional elements while considering boundary conditions. Its objective is to discretize and solve physical phenomena using simplified equations. Many researchers in the field of solar energy have employed the FEM to assess temperature and optimize the design of different solar module technologies such as CPV Flatcon [18], micromodule [19] and hybrid module [20]. Other researchers have used this method to evaluate solar cell temperature and estimate the cost of different heat sinks [21]. The Stationary Thermal Module of Ansys Workbench software was employed for FEM analysis in our subsequent work.

Similarly, the objective of this study is to use finite element modeling to guide the design of a CPV module based on SMT technology that was developed in [12]. For this purpose, a 4-solar cell CPV module prototype is fabricated using SMT assembly then experimentally characterized. Measurements are used to both assess the ability of the module to dissipate heat and validate a finite element model (FEM) through comparison to the predicted temperature distribution. Finally, using an extended version of the FEM, optimal dimensions of the module are determined in order to minimize cell temperature, ideally below 80°C.

II. Theoretical sections

The finite element thermal modeling of the CPV SMT module requires an understanding of the nature of the elements composing it, how these elements are assembled, the heat flux to be dissipated within this assembly, and the various modes of heat transfer within it.

The new CPV module presented in Fig. 1 uses SMT assembly to replace wire bonding for cell emitter connection. Figs 1-a and 1-b are not to scale. Fig. 1-a shows the simplified principle of the CPV module, where a Fresnel lens focusing light onto a solar cell soldered on a transparent glass PCB and protected by lamination layers. The assembly, consisting of the PCB, soldered solar cell, and lamination sheets, is called a bottom plate. Since the cell assembly process has been extensively detailed in [12], this section will exclusively focus on describing the bottom plate. Following the bottom plate description, we will examine the heat generation in this type of module and the various heat transfer modes associated with the CPV module.

1. Description of the SMT assembly concept of new CPV module

Fig. 1-b shows a cross-section of the bottom plate. While details of the assembly process development are described in [12], the bottom plate assembly is summarized as follows: The emitter contacts on the front face of the solar cell are soldered to a glass PCB through electrically conductive solder joints. The glass PCB contains metal tracks, covered with solder mask for non-soldered areas. The solder joints transfer the emitter contacts (-) onto the PCB. A transparent underfill fills the gap between the solar cell and the PCB to prevent reflections at the air/glass, glass/underfill, underfill/cell interfaces. Underfill fillets protect the sides of the solar cell to prevent short circuits and contribute to the thermomechanical stability of the assembly. The connection of the base contact is achieved through a metal ribbon/tape attached with electrically and thermally conductive epoxy. The epoxy also allows the transfer of the base contact (+) onto the metal tracks of the PCB, separated from the emitter tracks by the solder mask. Finally, the back face of the assembly is laminated with an EVA encapsulant and a Tedlar protective sheet to preserve the solar cells from the environment.

Now that we understand the SMT assembly of solar cells in a CPV module, let's explore how heat is generated in such a module and the various modes of heat transfer.

2. Heat generation and thermal transfer modes in a CPV SMT module

Using lenses to concentrate light on solar cells improves their efficiency but leads to significant power losses. This is because some of the direct normal irradiance (DNI) or incident power (P_{in}) does not reach the solar cell, and the concentrated light that does reach the cell is not fully converted into electricity. A part of the concentrated light is converted into heat. The module dissipates this heat into its surroundings. This paragraph analyses the process of heat generation, detailing the loss of light power when the luminous flux does not reach the cell. It also looks at the calculation of heat in the module and the associated heat transfer modes.

3. Optical losses in a CPV SMT module and heat flux generation in CPV SMT module

Fig. 2-a illustrates all the optical losses in a CPV SMT module using Fresnel lens (Silicon on Glass or SoG). Reflection losses occur at every surface with a change in refractive index. For a CPV SMT module using SoG Fresnel lens, reflections occur at the lens interfaces (air/glass, glass/silicone, silicone/air) and at the bottom plate interfaces (air/glass, glass/underfill, underfill/cell). Absorption represents a loss of power in a homogeneous medium. In the case of a CPV SMT module with SoG lens, some of the light is absorbed by the glass and silicone of the lens, as well as by the glass and underfill at the bottom plate. SoG lens, whether machined or polished, do not have a perfectly smooth surface due to the roughness naturally generated by the manufacturing processes, which induces to scattering losses.

Due to reflection, absorption and scattering losses, the incident light power (P_{in}) or Direct Normal Irradiance (DNI) does not reach the solar cell in its entirety. The light power received by the solar cell (P_{out}) is expressed as:

$$P_{out} = C_{geo} \times \eta_{optical} \times DNI \qquad (1)$$

where C_{geo} is the concentration factor of the lens on the solar cell, $\eta_{optical}$ is the optical losses, and DNI is the Direct Normal Irradiance. Part of the light Pout is converted into electricity, while another part is converted into heat. The heat, known as $Q_{th,in,pmpp}$, is calculated using the following expression:

$$Q_{th,in,pmpp} = C_{geo} \times \eta_{optical} \times DNI \times (1 - \eta_{electrical}) \qquad (2)\ [18]$$

where $\eta_{electrical}$ is the electrical efficiency. The heat $Q_{th,in,pmpp}$ present in the CPV SMT module must be dissipated to the surrounding environment.

Having looked at all the optical losses and heat generated in the module; the next section explores the different modes of heat transfer possible in the CPV SMT module.

4. Heat transfer modes in a CPV SMT module

There are three heat exchange mechanisms in a CPV SMT module: conduction, convection, and radiation. Fig. 2-b illustrates these three modes of heat transfer.

Thermal conduction: heat circulates through the solar cell and the media in close contact with the solar cell. Heat is transferred by conduction through the vibration of the lattice and the migration of electronic charges in the case of metals. Consequently, a good electrical conductor is a good heat conductor. Thermal conduction is governed by Fourier's law:

$$\theta = \frac{L}{K.A} = \frac{\Delta T}{Q_{conduction}} \qquad (3)$$

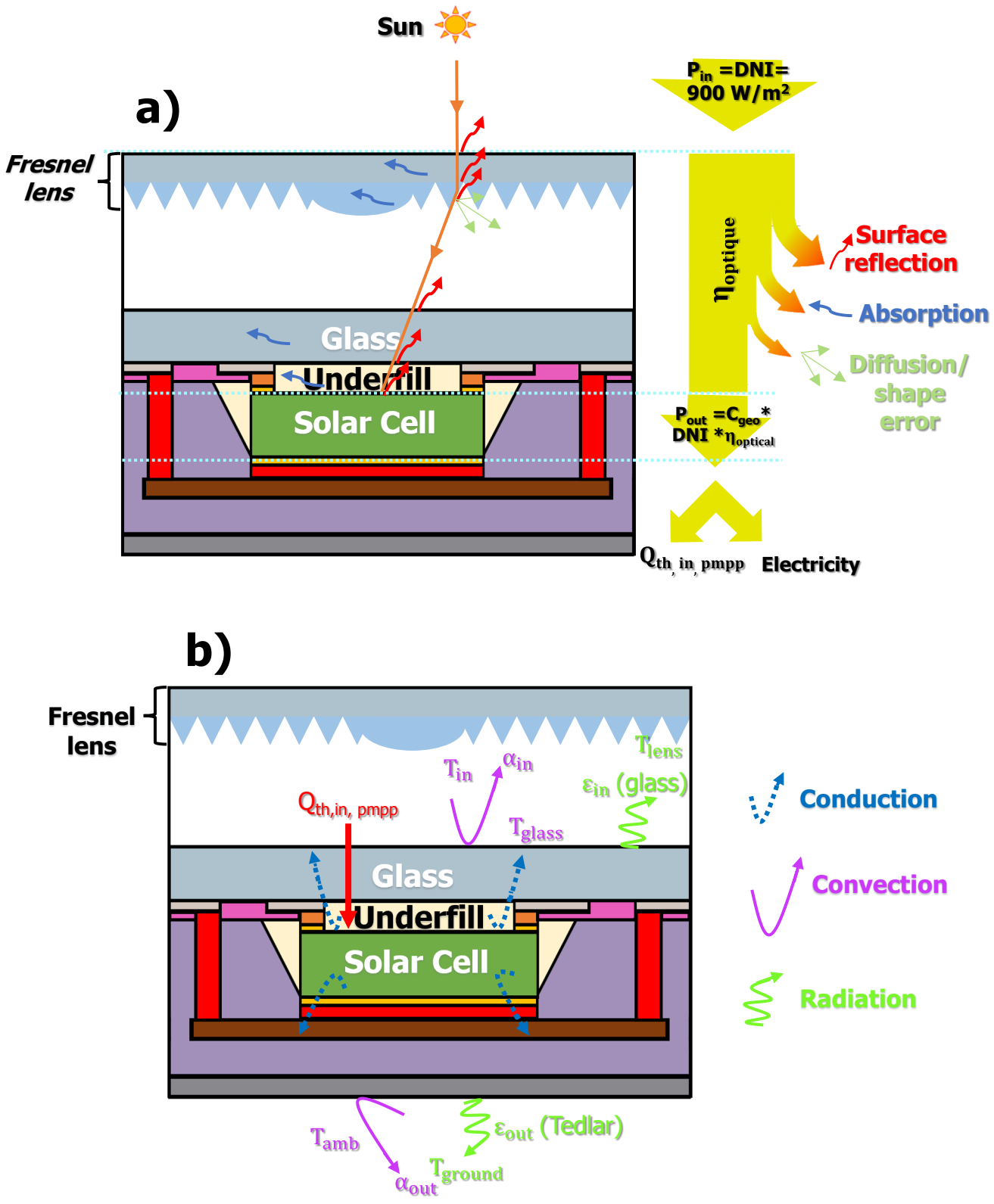

Fig. 2. a) Schematic of optical losses in a CPV SMT module. b) Schematic of heat transfer modes in a CPV SMT module.

with θ the thermal resistance, L the thickness of the material, K the thermal conductivity, A the surface area of the

material, ΔT the variation in temperature along L, $Q_{conduction}$ is the conduction heat transfer rate. Thermal resistance is inversely proportional to thermal conductivity and the surface area of the material. In other words, the higher the thermal conductivity and/or surface area of the material, the better it dissipates heat.

Thermal convection: This involves the transfer of heat between the fluid inside the module (air) and the glass surface of the bottom plate, as well as between the rear face of the bottom plate (Tedlar) and the ambient air. Thermal resistance, in the case of convection, is inversely proportional to the convection heat transfer coefficient and the surface area of the material:

$$R_{convection} = \frac{1}{\alpha . A} = \frac{\Delta T}{Q_{convection}} \qquad (4)$$

where $R_{convection}$ is the thermal resistance, A is the material (glass or Tedlar in our case) surface, $Q_{convection}$ is the convection heat transfer rate, ΔT is the temperature difference between the surface of the glass (T_{glass}) and the air inside the module (T_{in}) or the temperature difference between the surface of the Tedlar (T_{Tedlar}) and the ambient air (T_{amb}), and α is the convective heat transfer coefficient. α depends on the temperature, fluid speed, fluid viscosity, heat flow, surface roughness, type of flow (single-phase/biphase) and laminar or turbulent flow, angle of inclination, wind speed, etc [22]. In Fig. 2-b, α_{in} et α_{out} represents respectively, the convective heat transfer coefficient inside and outside the module. T_{in} and T_{amb} are the temperature inside the module and the ambient temperature respectively.

Thermal radiation: heat is transferred by electromagnetic emission, mainly in the infrared wavelengths between the lens and glass of the bottom plate and Tedlar and ground. The radiant energy emission rate is defined by the following expression:

$$R_{radiation} = \varepsilon . \sigma . A . \left(T_i^4 - T_j^4\right) = Q_{ij} \qquad (5)$$

with $R_{radiation}$ the radiant energy emission rate, ε the emissivity of the materials (glass and Tedlar), σ the Stephan-Boltzmann constant, A is the radiated surface area, $T_i^4 - T_j^4$ is the temperature difference between the surface of the glass and the lens or the temperature difference between the surface of the Tedlar and the ground. In Fig. 2-b, ε_{in} et ε_{out} represents respectively, the emissivity of the glass and the Tedlar. T_{lens} and T_{ground} are the temperature of the lens and the ground respectively.

In this Section II, we have identified the components of the CPV SMT module and their assembly. Consequently, we can easily define the geometry of the CPV SMT module for the model, along with the materials associated with each solid in the geometry. The heat flux ($Q_{th,in,pmpp}$) to be dissipated in the CPV SMT module can also be calculated, with the various parameters of the $Q_{th,in,pmpp}$ expression (2) measured experimentally. The different heat transfer modes within the CPV SMT module are known and serve as boundary conditions in the modeling. Other parameters such as T_{in}, T_{amb}, T_{ground}, and T_{lens}, also boundary conditions, are likewise measured experimentally.

The following section III aims to assess the CPV SMT module's heat dissipation capability and validate a finite element model (FEM). To achieve this, a CPV SMT module was manufactured and characterized under actual operating conditions. The parameters of expression (2), obtained experimentally, along with temperatures (T_{in}, T_{amb}, T_{ground}, T_{lens}) measured experimentally, were input into the finite element model. The temperature distribution predicted by the

model on the rear face of the bottom plate (Tedlar) was compared to that measured experimentally by the IR camera. Subsequently, the finite element model was employed to deduce the temperature of the solar cells.

III. Experimental and results sections

1. Description of the 4-solar cell module prototype

Fig. 3-a presents a top view of the bottom plate in the CPV SMT module, composed of a PCB. This PCB is manufactured with a glass substrate on which copper metal tracks form grids. Fig. 3-a illustrates two types of metal tracks: those dedicated to the emitter (-) contacts of the solar cell and those intended for the base contact (+) reporting of each solar cell. These two types of metal tracks are electrically separated and covered by a solder mask, as indicated in Fig. 3-b. On the PCB, 4 triple-junction III-V/Ge solar cells (A, B, C, D) are soldered, each having an active surface area of 8.751 mm². These solar cells are independent and not interconnected with each other. Fig. 3-b and 3-c respectively show an enlarged top view and rear view of a solar cell soldered on the PCB without EVA and Tedlar. After soldering the 4 solar cells onto the PCB, copper ribbons were adhered to the back (base contact +) of each solar cell. Each ribbon was then connected to the PCB's metal tracks (+), as depicted in Fig. 3-d. To fill the space between the PCB and each copper ribbon, pre-cut EVA encapsulant sheets of the same dimensions as the copper ribbons were used. Adherence of the ribbon to the base contact of the solar cell and the connection of the ribbon to the metal track were ensured by an electrically conductive adhesive. Electrical wires were soldered onto the metal tracks (+) and (-) to enable subsequent characterization of each solar cell, as illustrated in Fig. 3-d. Fig. 3-e presents a top view of the reverse side of the bottom plate, where an encapsulant EVA lamination and a Tedlar protective sheet are observed. The surface of the EVA and Tedlar lamination is slightly smaller than that of the PCB to ensure perfect planarity of the bottom plate in the module. The lamination was carried out on a hot plate under atmospheric pressure in the absence of a laminator in

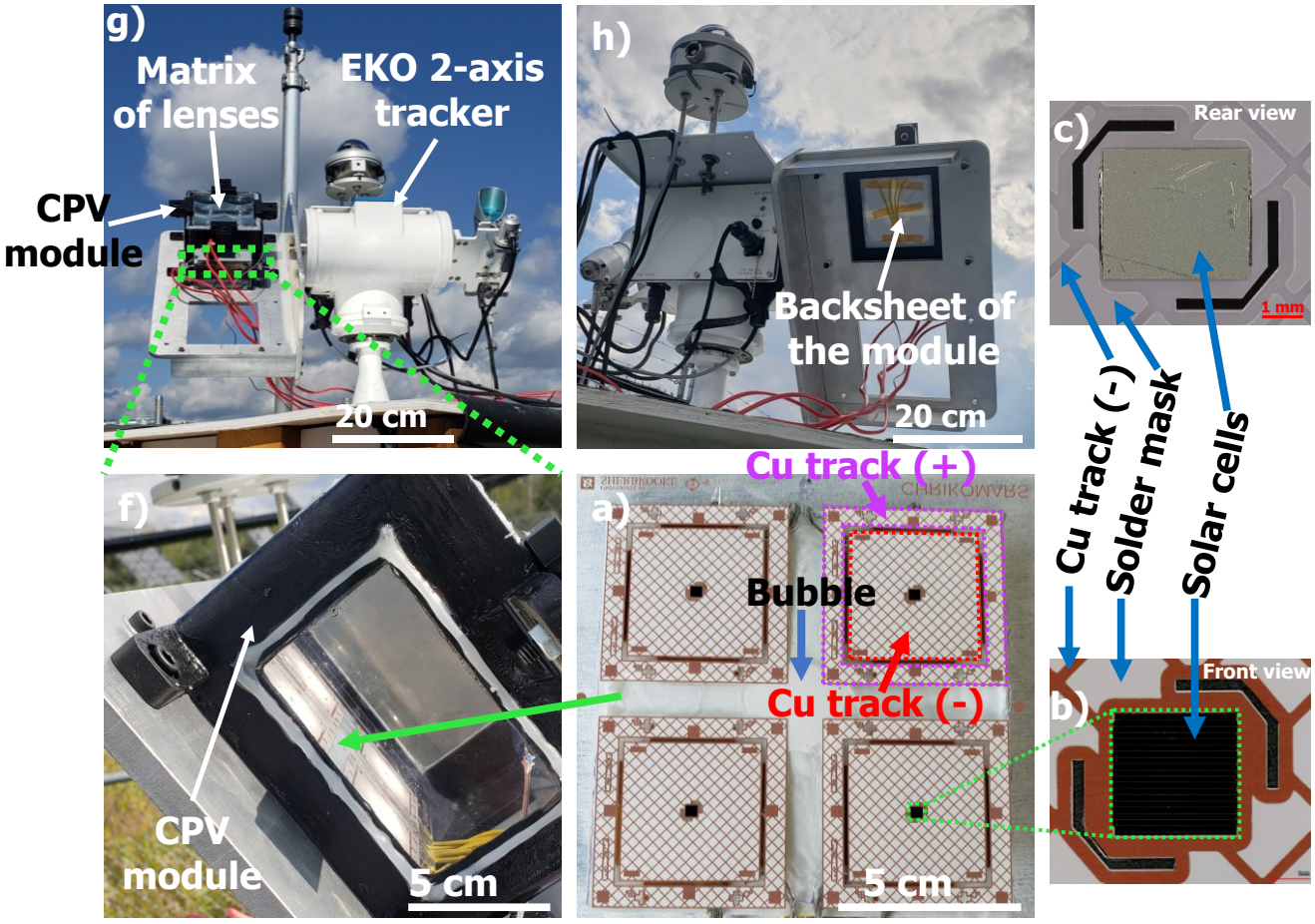

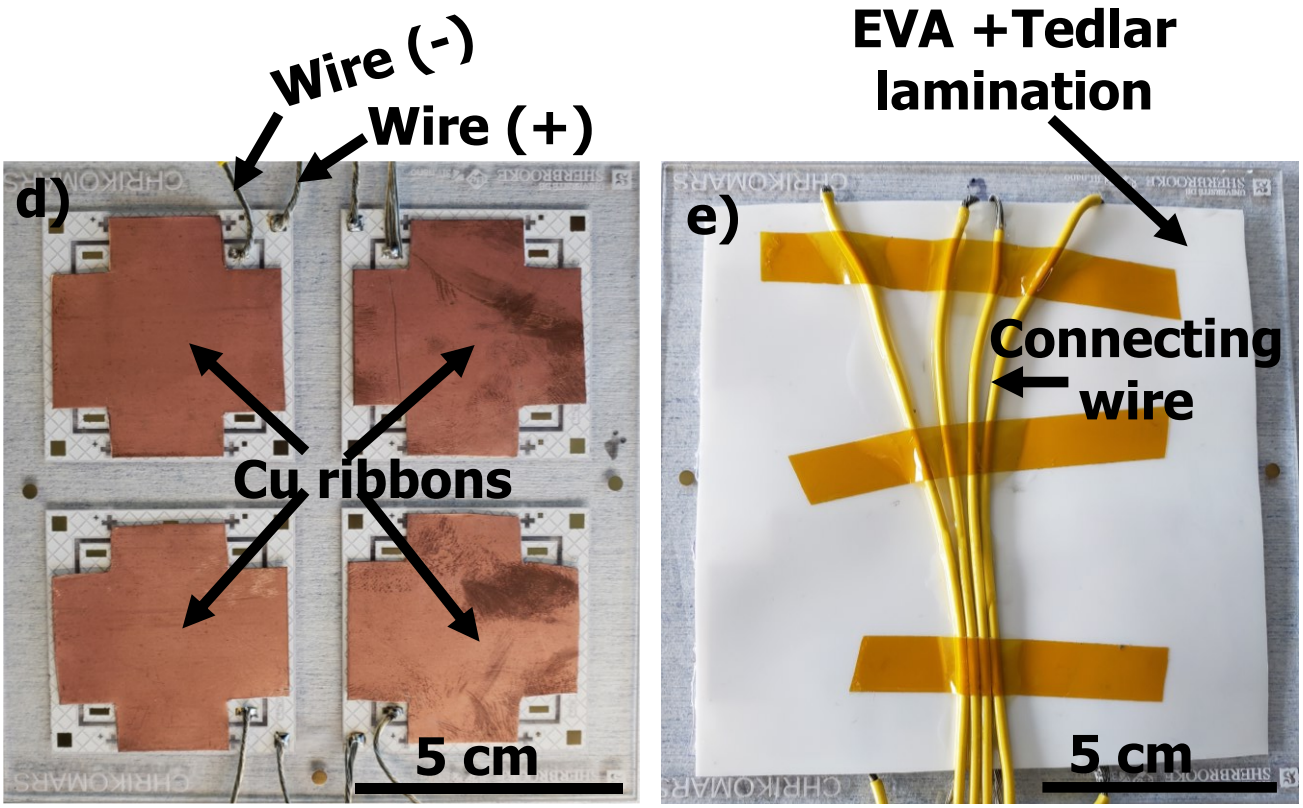

Fig. 3. a) Top view of the bottom plate in the CPV SMT module, b) enlarged top view of a solar cell soldered on the PCB without EVA and Tedlar lamination, c) enlarged rear view of a solar cell soldered on the PCB without EVA and Tedlar lamination, d) back side of the bottom plate showing the Cu ribbons glue behind each solar cell, e) back side of the bottom plate showing the lamination by the EVA and Tedlar, f) zoom on the bottom plate placed inside the CPV module, g) CPV module mounted on the EKO Keithley 2-axis tracker, h) back side of the CPV module mounted on the EKO Keithley 2-axis tracker.

the laboratory, leading to the formation of bubbles at the center and other locations of the bottom plate, as depicted in Fig. 3-a. The presence of these bubbles could compromise the thermal conduction in the affected areas of the bottom plate. However, only the central region of the bottom plate displays a substantial bubble, accompanied by a few small regions surrounding the center featuring smaller bubbles. Consequently, the temperature distribution in the areas where the solar cells are located is reliable. Additionally, yellow connecting wires are visible on the reverse side of the bottom plate. The manufactured bottom plate is then integrated into the module and the edges are sealed from the bottom to prevent moisture from entering the module. Fig. 3-f provides an enlarged view of the module's interior. A matrix of 4 lenses aligned opposite each solar cell is fixed at 93 mm above the bottom plate, as depicted in Fig. 3-g. The 4-cell CPV SMT module is mounted on a 2-axis EKO solar tracker from the Helios platform at the University of Sherbrooke, as shown in Fig. 3-g. The rear of the module mounted on tracker is shown in Fig. 3-h.

The 4-cell CPV SMT module, mounted on the 2-axis EKO tracker, underwent electrical characterization using a Keithley instrument in the Helios platform at the University of Sherbrooke. This electrical characterization involved current-voltage (I-V) measurements of each individual solar cell to deduce their respective electrical efficiency. Additionally, temperature distribution on the rear face of the bottom plate (Tedlar), $\mathbf{T_{in}}$, $\mathbf{T_{amb}}$, $\mathbf{T_{ground}}$ and $\mathbf{T_{lens}}$ were experimentally measured using thermocouples and an infrared camera. The details of these characterizations are described in the following paragraphs.

2. Electrical characterisation of the module under real operating conditions

The tracker on which the module is mounted is controlled by a Raspberry Pi microcomputer with an implemented tracking program. The Raspberry Pi also controls a Keithley multiplexer (3706A) and a Keithley source/measurement unit (2601B) to measure the electrical characteristics (current-voltage or I-V) of each solar cell [23]. The IEC62670-3 (International Electrotechnical Commission) [24] and ASTM E2527 (American Standards of Technical Material) [25] standards were respectively used for characterization under standard conditions (DNI of 900 $W.m^{-2}$, Wind speed of 2 $m.s^{-1}$, and AM1.5D spectrum) and data filtering (ambient temperature should be comprised between 10°C and 30°C, DNI should be more than $750W.m^{-2}$, rejecting data if DNI deviation is more than 2% within 10 minutes, rejecting data if diffuse radiation is above $140W.m^{-2}$). The current-voltage (I-V) characterization procedure begins with the measurement of the open-circuit voltage (V_{OC}), followed by a sweep of the cell voltage in the range from 0 V to V_{OC}. The sweep is conducted in eight linear points between 0 V and 70% of V_{OC}, then in sixteen points between 70% and 95% of V_{OC}, and finally in eight points between 95% of V_{OC}. This process results in a total of thirty-two cell current values distributed over a voltage vector. The characterization of each cell, including tracker positioning and measurement, takes approximately 10 seconds.

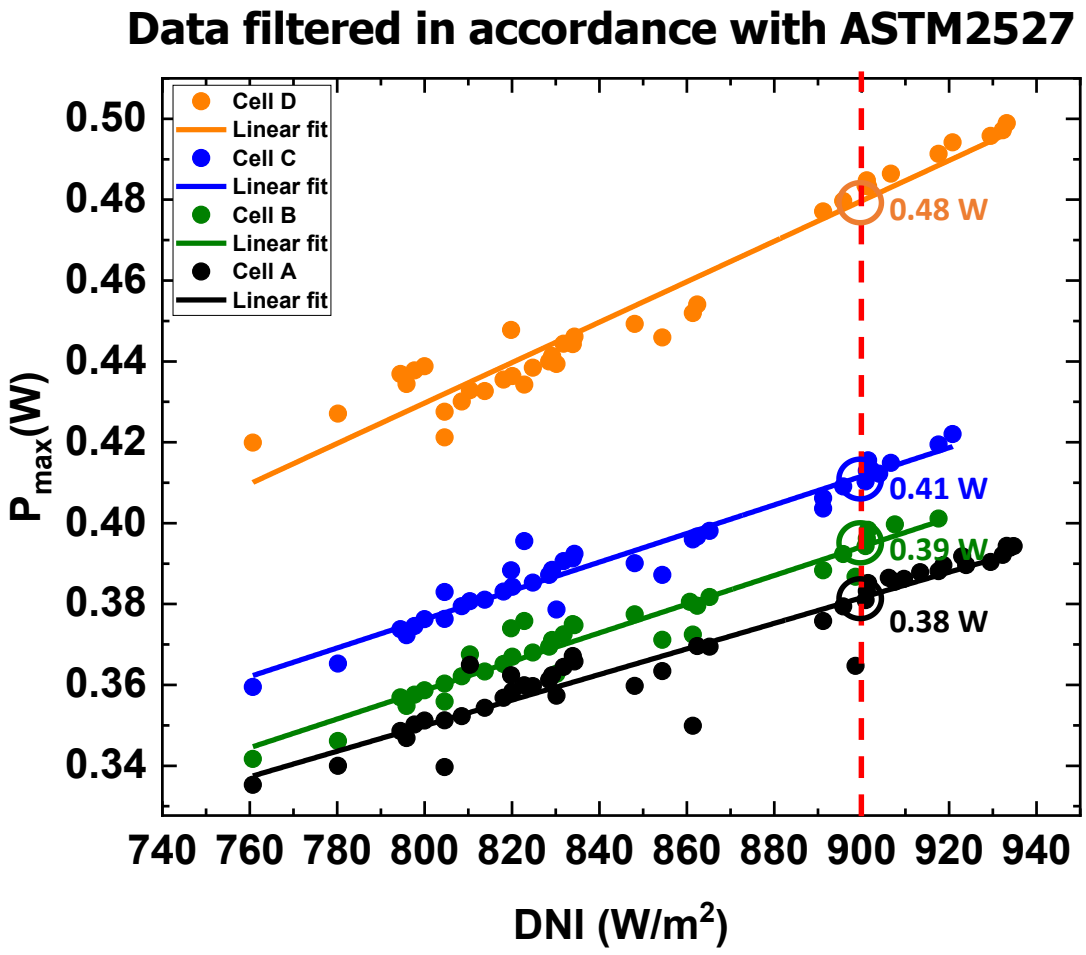

Fig. 4. Maximum power of solar cells A, B, C and D in modules as a function of Direct Normal Irradiance (DNI) extracted from current-voltage (I-V) measurements [29].

Table 1: Material dimensions used in the 4-cell CPV prototype module. L, l and e represent respectively the length, width, and thickness.

Layer of CPV module	Material	Isotropic thermal conductivity (W/m.K)	Dimensions (L × l × e) mm^3
Glass	Tempered	1.8	124.29 × 124.29 × 2
Metal on the glass	Copper	399	61.71 mm^2 × 0.035 mm
Solder joint	SAC305	60	2.49 × 0.20 × 0.075
Underfill	Sylgard 184	0.27	3 × 3 × 0.075 and 1.5 mm filet
Solar cell	Germanium	60	3.4 × 3 × 0.18
Metal ribbon	Copper	399	1524.39 mm^2 × 0.5 mm
Conductive adhesive	Conductive epoxy	85	3.4 × 3 × 0.075
Encapsulant	EVA	0.35	114,29 × 114.29 × 0.35
Backsheet	Tedlar	0.2	114,29 × 114.29 × 0.20

Table 2: Temperature values, emissivity and convection coefficients, efficiency under concentration of solar cells used for the finite element model of the CPV module with 4 solar cells. The temperature for efficiency measurement is 38 °c, and the direct normal solar irradiance (DNI) is 926.6 ± 7.4 w/m².

Convection coefficient (α)	$\alpha_{out} = 9W/(m^2.K)$
	$\alpha_{in} = 7W/(m^2.K)$
Emissivity coefficient (ε)	$\varepsilon_{Teldar} = 0.94$
	$\varepsilon_{Glass} = 0.96$
Temperature	$T_{ambient} = 20°C$
	$T_{in} = 36.4°C$
	$T_{ground} = 18°C$
	$T_{lens} = 25°C$
Cell A efficiency	30.28%
Cell B efficiency	31.28%
Cell C efficiency	32.66%
Cell D efficiency	38.07%

I-V measurements are utilized to extract the maximum power from solar cells A, B, C, and D in the module as a function of Direct Normal Irradiance (DNI). DNI measurements were conducted simultaneously with the I-V

measurements using a pyrheliometer located on the tracker. Fig. 4 presents the relationship between the maximum power (P_{max}) and DNI for these cells in the module [26]. The points on the graph represent powers extracted from the I-V measurements, and the lines indicate linear regressions. As expected, a linear variation of maximum power is observed. Analyzing the graph of maximum power as a function of DNI, P_{max} values corresponding to a DNI of 900 W/m² are deduced for each solar cell as recommended in the IEC62670-3 standard. These P_{max} values at 900 W/m² are 0.38 W, 0.39 W, 0.41 W, and 0.48 W, respectively, for cells A, B, C, and D in the module. The electrical efficiencies of the solar cells are calculated using the following Equation (6):

$$\boldsymbol{\eta_{electrical} = \frac{P_{max}(at\ 900\ W/m^2)}{DNI \times A_{cell} \times C_{geo}}} \qquad (6)$$

Using C_{geo} = 160, the concentration of the lenses in the manufactured CPV SMT module prototype ($\boldsymbol{\eta_{optical}}$ of these lenses is 92%), DNI = 900 W/m^2 (Direct Normal Irradiance), A_{cell} = 8.751 mm^2 the active surface area of each solar cell, and P_{max} (W) the maximum power of each solar cell at 900 W/m^2, the calculated efficiency values are 30.28%, 31.28%, 32.66%, and 38.07% for the A, B, C, and D, respectively. The efficiencies vary due to form errors associated with lens manufacture.

With electrical measurements completed, let us proceed to the experimental temperature measurements.

3. Experimental temperature and emissivity measurements; tabulated convection coefficient

Following the electrical measurements, temperature measurements under actual operating conditions were conducted on the CPV SMT module. The measurement was taken in the early afternoon after the module had been running since sunrise.

As the solar cell is fully encapsulated and inaccessible, we measured the temperature of the backside of the bottom plate using an IR camera, i.e., the temperature of the Tedlar sheet, to compare it to that predicted by FEM. The IR camera used is the FLIR E54 from Teledyne, calibrated by the company with an accuracy of ±2°C before measurements. But to ensure the reliability of our temperature measurements, three calibration methods were employed. Firstly, a laminated glass sample with EVA and Tedlar was heated on a hot plate, and the temperature was measured by a thermocouple and validated by the IR camera. Secondly, ambient temperature calibration was performed by measuring the outdoor temperature to verify its correspondence. Finally, once the temperature variations of the bottom plate (Tedlar) were captured by the IR camera to generate a thermal image, the emissivity value of the Tedlar provided by the camera was compared to the literature [27], confirming agreement. Indeed, the camera directly measures the emissivity of the Tedlar, and this infrared radiation emitted by the Tedlar and detected by the camera is directly linked to a specific temperature displayed on the thermal image. Fig. 5-a show an IR camera image obtained from the rear Tedlar of the prototype, with the measured temperatures displayed on a color bar. The maximum and minimum measured temperatures (T_{max}(IR) and T_{min}(IR) respectively) are 37.9±2°C and 20.5±2°C, respectively. The temperature displayed in the upper left corner of the image represents the temperature in the center (T_{cen}(IR)) of the IR image and is 23.1°C.

The temperatures T_{lens}, T_{amb}, and T_{ground} were also measured using an IR camera, with respective values of 25°C, 20°C, and 18°C. A type T thermocouple, integrated during the prototype fabrication, measures the internal temperature (T_{in}) of the module and the value measured is 36.4°C.

During these above-mentioned experimental temperature measurements, the measured DNI by the pyrheliometer was 926.6 ± 7.4 W/m^2.

The emissivity measured by the IR camera for Tedlar and glass is 0.94 and 0.96, respectively. As stated in Section II, calculating the convection coefficients is complex due to its dependence on various parameters. Most researchers

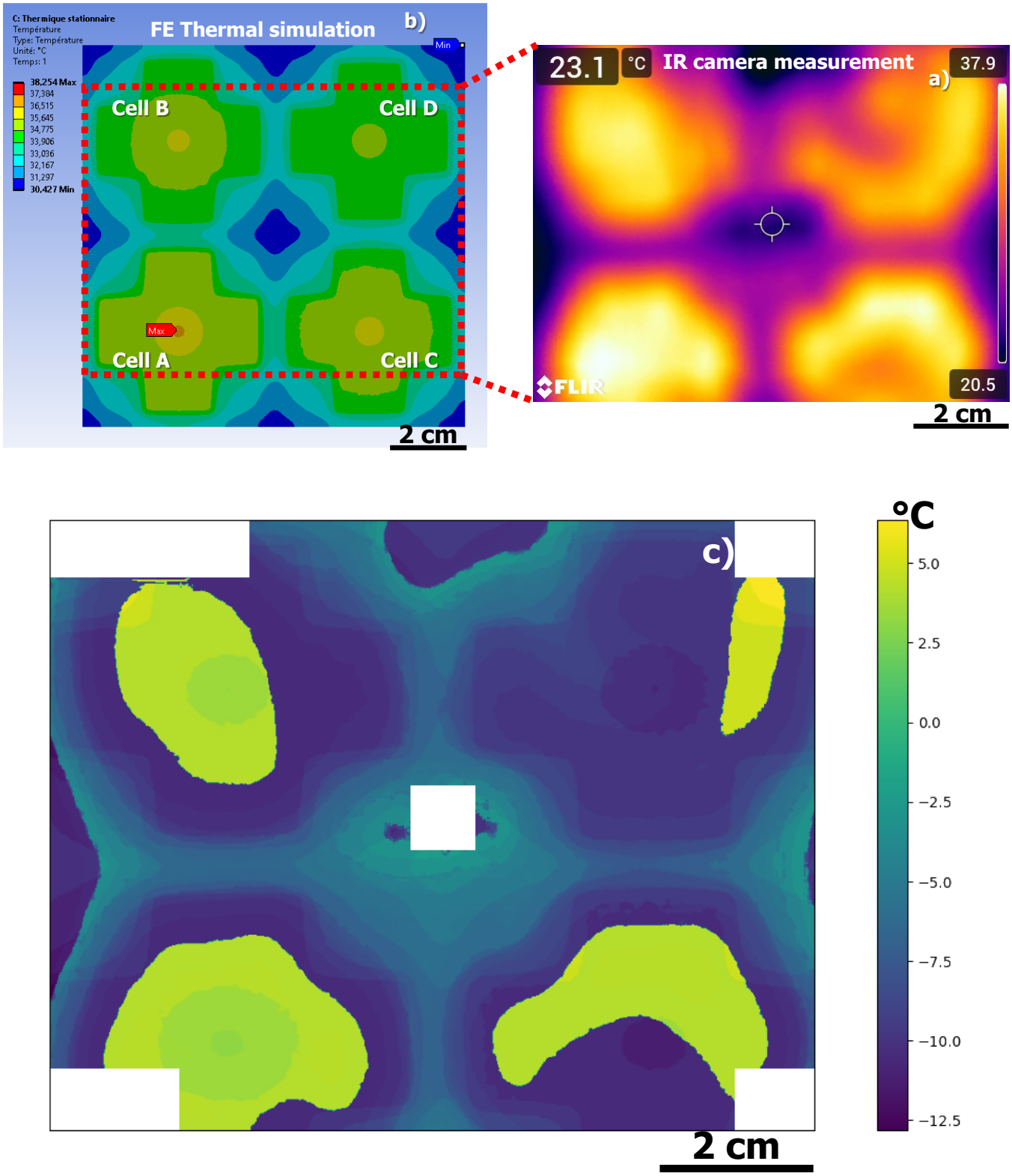

Fig. 5. a) Results of the thermal simulation of the 4 solar cell model, b) experimental measurements of the backsheet temperature using the IR camera, c) Difference between the temperatures at each point of the IR camera image and the FEM model called "Delta image".

suggest values ranging between 1 and 10 for natural convection in air [19], [28], [29]. Any value within this range is

considered acceptable, and differences between results are negligible. In our simulations, we assume values of 9 $W/m^2 \cdot K$ for external surfaces and 7 $W/m^2 \cdot K$ for internal surfaces, in accordance with the literature [19]. All these experimental temperature, emissivity, and convection data are recorded in Table 2. The thermal conductivity, an intrinsically stable property for each material of the bottom plate typically provided by suppliers, is also listed in Table 2.

All the experimental parameters required for the calculation of $Q_{th,in,pmpp}$ are currently available. Boundary conditions, including temperatures, emissivities, convection coefficients, and thermal conductivity are now known. These data will be incorporated into the finite element thermal simulation model, which will be developed in the next section.

4. Description and results of finite element thermal modeling

For the steady-state thermal analysis, the Stationary Thermal Module of the Ansys Workbench software was used for the simulation. The model, shown in isometric view in Fig. 6-a and b emulate the 4-cell prototype whose dimensions are given in Table 1 along with the thermal conductivities of each material. Only the bottom plate considered. The hybrid mesh is composed of cube and prism elements. The number of elements and nodes used for the simulation here are 61245 and 206237, respectively. The concentrated heat on each solar cell, $Q_{th,in,Pmpp}$, was calculated using the experimental efficiencies of each solar cell in the prototype. The geometric concentration factor, C_{geo}, used in the calculation of $Q_{th,in,Pmpp}$, corresponds to that of the prototype, which is 160×, indicating that the lens concentrates direct normal irradiance on the solar cell 160 times. The optical efficiency η_{opt} used in the calculation of $Q_{th,in,Pmpp}$ is that of the prototype, assessed at 0.92 due to optical losses in the module, meaning that 92% of the DNI effectively reaches the solar cell. Indeed, the low optical loss of 8% of the lens is due to the use of low-iron glass for its fabrication, which promotes better transmission of all wavelengths of the solar spectrum. Additionally, the optical system is treated

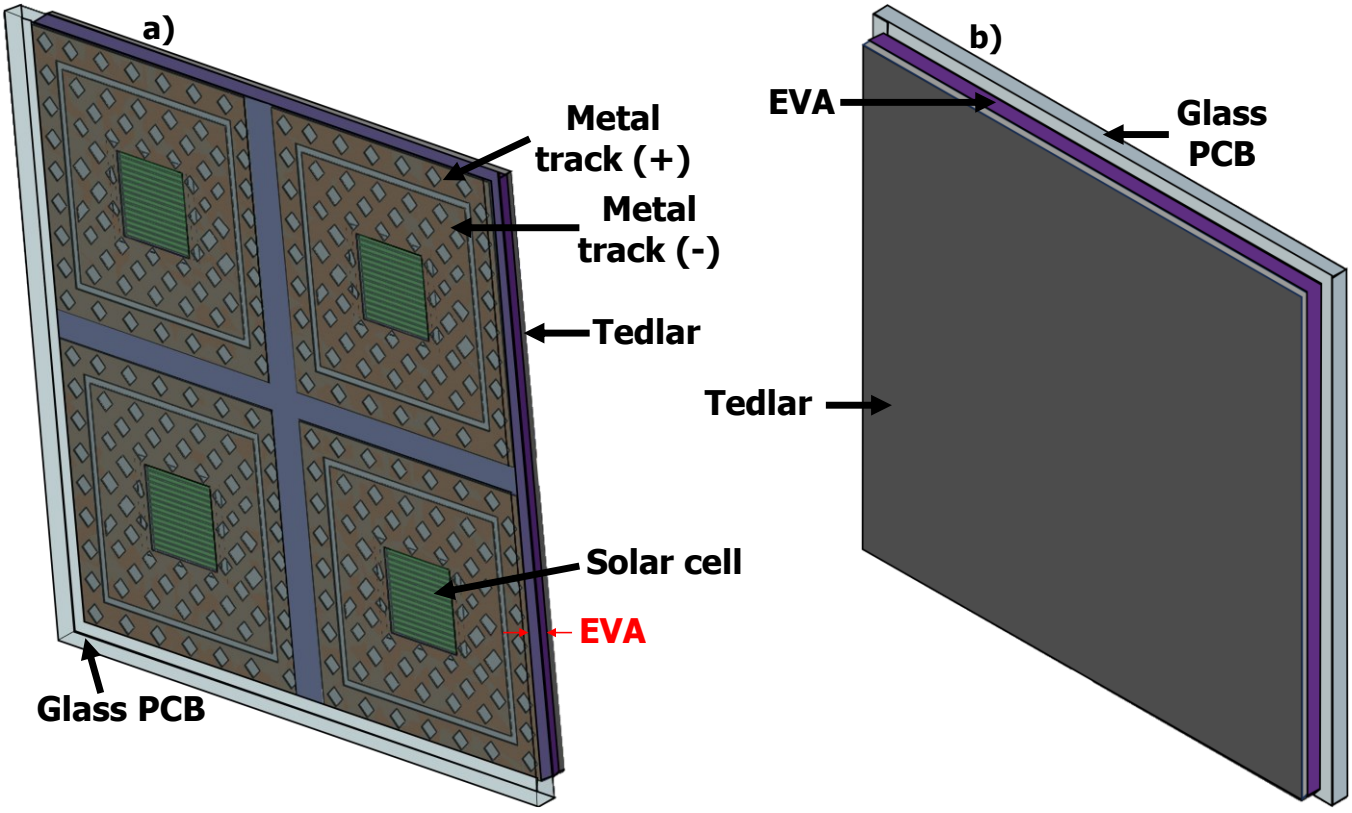

Fig. 6: Isometric view of the 4 solar cell model of the CPV module bottom plate. a) Isometric view of the front face of the bottom plate. b) Isometric view of the back face of the bottom plate.

with an anti-reflective coating to limit reflections. Moreover, the thicknesses of PDMS and glass are optimized so that light absorption in these materials is negligible. Furthermore, the low roughness of the lens surface restricts the diffusion of light at its surface. The DNI used for the calculation of $Q_{th,in,Pmpp}$ is the value measured by the pyrheliometer, assessed at 926.6 ± 7.4 W/m^2. The calculated heat for each solar cell was applied to the corresponding front surface in the model. Heat propagates through the module's bottom plate via conduction, while the bottom plate exchanges heat with the surrounding environment through convection and radiation. The modeling incorporates conduction through the thermal conductivity assigned to each material. Convection and radiation are applied to the front surface of the bottom plate (glass) and the back surface of the bottom plate (Tedlar). In practice, the modeling considers convection on the front surface of the bottom plate (glass) and the back surface of the bottom plate (Tedlar) using respectively the convection coefficients α_{in}, with the temperature T_{in} inside the module defined as boundary conditions, and α_{out} with the ambient temperature T_{amb} defined as boundary conditions. Similarly, radiation on the front surface of the bottom plate (glass) and the back surface of the bottom plate (Tedlar) is considered, respectively, through the emissivity of the glass (ε_{Glass}) with the temperature T_{lens} as boundary conditions and the emissivity of the Tedlar (ε_{Tedlar}) with the temperature T_{ground} as boundary conditions. The 4 III-V/Ge triple-junction solar cells are each considered as a germanium chip due to the very thin thickness of the III-V material (~10 µm) compared to that of germanium (~170 µm). The geometric model used in this simulation also does not include the solder mask due to its very thin thickness (~3 µm). Fig. 5-b shows the temperature distribution on the Tedlar of the 4-cell module obtained by FEM. According to Fig. 5-b, the maximum and minimum temperatures (T_{max}(FEM) and T_{min}(FEM)) of the Tedlar are 38.3°C and 30.4°C respectively. The temperature of the center of the FEM image (T_{cen}(FEM)) is also around 30.4°C.

After the fabrication of the CPV SMT module and the electrical and thermal characterizations, along with finite element thermal modeling based on experimental data, the next section will focus on the discussion and comparison of the experimentally obtained results with the modeling.

IV. Discussion of experimental results and modeling

The FEM results, depicted in Fig. 5-b, show distinct temperature profiles for each solar cell. This thermal disparity arises from the different efficiencies of the solar cells. Indeed, the less efficient the solar cell, the higher the heat flux $Q_{th,in,pmpp}$ that needs to be dissipated. The T_{max}(FEM) is located under cell A. This location for T_{max}(FEM) is due to the relatively low efficiency under concentration of cell A (30.28%) compared to other cells (31.28%, 32.66%, 38.07% respectively for cell B, C and D) and thus the high amount of heat that must be dissipated. These results align with the IR camera measurements presented in Fig. 5-a.

The T_{min}(IR) and T_{cen}(IR) temperatures are respectively 20.5°C and 23.1°C. Moreover, these temperatures are lower than the interior temperature (T_{in} = 36.4°C) measured separately, which confirms the ability of the CPV module to efficiently dissipate heat. The measured T_{max}(IR) is the same as the simulation T_{max}(FEM). However, the measured T_{min}(IR) and T_{cen}(IR) are significantly different from simulation T_{max}(FEM) and T_{min}(FEM). To have a better insight on the temperature discrepancy, Fig. 5-c shows the temperature difference at each point of the IR camera and FEM model images, called "Delta image". The white areas correspond to the regions of the IR camera image showing the temperatures and the cursor in the center. These regions have been removed from "Delta image" because they are physically unusable. The minimum and maximum values of "Delta image" are -12.5°C and 6.4°C respectively, with a mean value of 5.7°C and a standard deviation of 5.5°C. We hypothesize that this difference of 5.7±5.5°C between the FEM model and the IR camera can be attributed to the bubbles present in the bottom plate, and the electrical connection wires. As mentioned earlier, the presence of bubbles leads to poor thermal conduction in the affected areas, resulting in higher temperature as the bubble increases. Moreover, the presence of wires can compromise heat exchange with the environment. In the prototype, the bubble is more pronounced at the center of the bottom plate, and the passage of electrical wires through this area could account for the higher temperature at that location (T_{cen}(IR)) compared to the minimum temperature (T_{min}(IR)).

Considering these explanations and the fact that the FEM accurately predicts T_{max}, including a higher T_{max} for the least efficient solar cell A, we can state that the FEM model matches well with the experimental one.

The thermal distribution on each solar cell, obtained from the simulation, is presented in Appendix 1. The maximum temperature deduced from this simulation reaches approximately 38 °C for all four solar cells. However, the temperature distribution on the cells is not uniform. Specifically, on cell D, the most efficient one, only a small area reaches the temperature of 38 °C, while the rest of the cell reveals a thermal gradient, with the lowest temperature approaching 36 °C. In contrast, on cell A, the least efficient one, almost the entire cell records a temperature of 38 °C. Therefore, we consider that the operating temperature of the solar cells in the CPV SMT prototype is well below 80 °C.

After validation of the model, we will extend in the following section, the FEM model to a large scale and undertake a parametric study to guide the design of a large module.

V. Parametric study

The experimental data of the 4-cell module prototype validates the simulation model. However, the dimensions (surface area, thickness) of the materials used to manufacture the 4-solar cell module were chosen based on what is available in our laboratory. It is possible to modify these dimensions and/or the nature of the materials, which could lead to a reduction in the weight and cost of SMT assembly. To optimally accomplish this while still respecting the need to maintain maximum solar cell temperature below 80°C, it is important to do so using a more representative operating environment. We therefore extended our FEM study to large scale modules that typically comprise 200 solar cells.

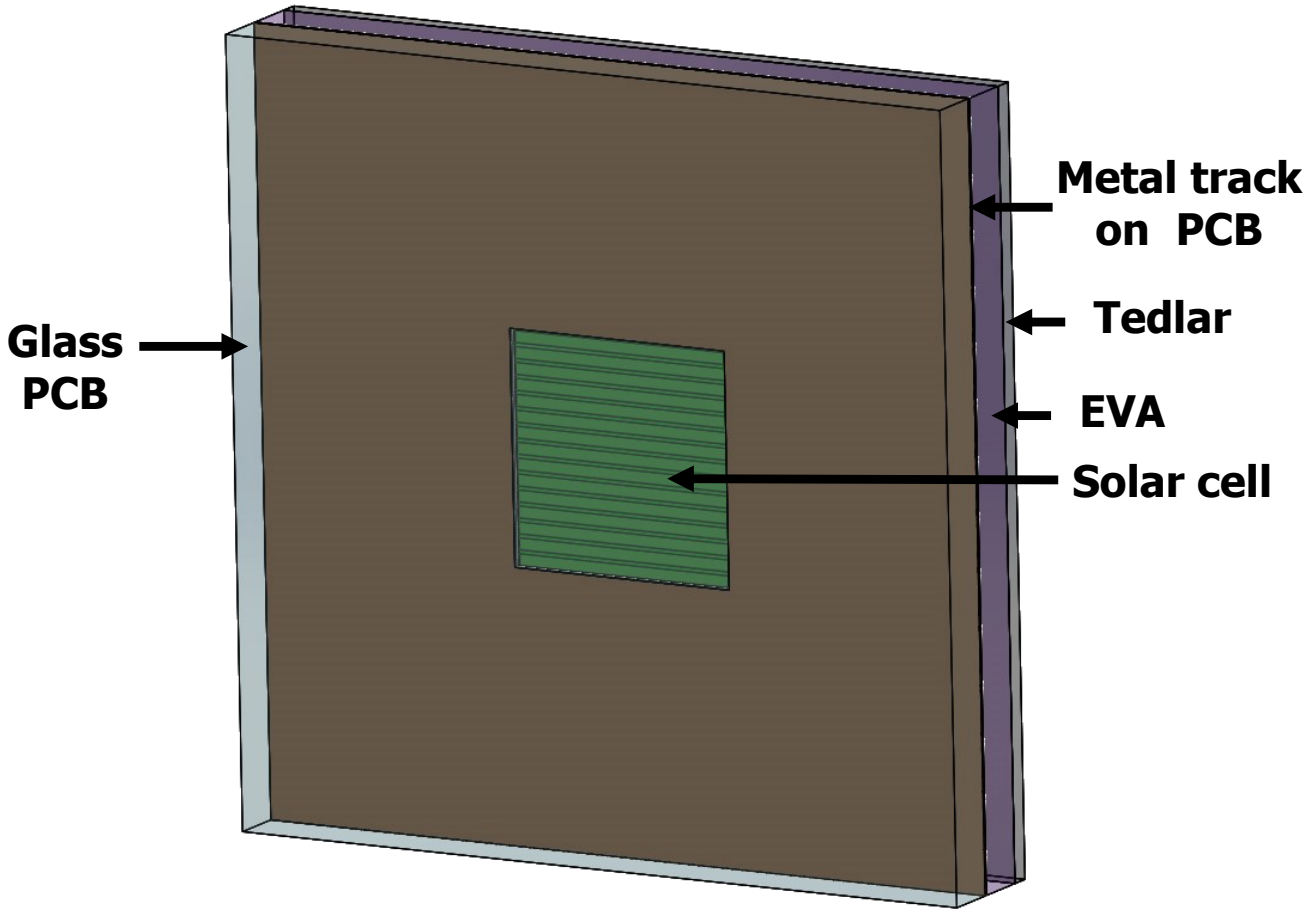

Fig. 7. Isometric view of the front face of the infinite-scale model of the CPV module's bottom plate.

Table 3: Taterials and thermal conductivity used for the finite element model for large scale module [18], [30].

Layer of CPV module	Material	Isotropic thermal conductivity (W/m.K)		Baseline dimensions (L × l × e) mm^3
Glass PCB	Tempered glass	1.8		57.143 × 57.143 × 2
metal on the glass	Copper	399		57.143 × 57.143 × 0.035
Solder joint	SAC305	60		1.49 × 0.2 × 0.075
Underfill	Sylgard 184	0.27		3.4 × 3 × 0.075
Solar cell	Germanium	60		3.4 × 3 × 0.180
Metal ribbon	Aluminium alloy	173.15K	114	41× 41 × 0.5
		273.15K	144	
		373.15K	165	
		473.15K	175	
	Copper	399		41 × 41 × 0.5
Electrically conductive adhesive	Conductive epoxy	85		3.4 × 3 × 0.05
Encapsulant	EVA	0.35		57.143 × 57.143 × 0.35
Backsheet	Tedlar	0.2		57.143 × 57.143 × 0.2

Table 4: Temperature values, emissivity and convection coefficients used for the finite element model for large scale module. The efficiency is considered to be 40%, measured at 25°c with an AM1.5d spectrum (DNI = 900 w/m^2).

Convection coefficient (α)	$\alpha_{out} = 9 W/(m^2.K)$
	$\alpha_{in} = 7 W/(m^2.K)$
Emissivity coefficient (ε)	$\varepsilon_{Teldar} = 0.94$
	$\varepsilon_{Glass} = 0.96$
Temperature	$T_{ambient} = 27.7°C$
	$T_{in} = 52°C$
	$T_{ground} = 23°C$
	$T_{lens} = 37.5°C$

1. Description of the FEM model for large-scale module

To emulate the large-scale module, we model single cell mono-modules then fix boundary conditions (Isotropic thermal conductivity) to mimic the presence of identical mono-modules at each adjacent side (equivalent to an infinite module). A isometric view of the simulation model is shown in Fig. 7. In this model, the metal on the PCB is arranged continuously on the glass, except for the active area of the solar cell, to simplify the model compared to the previous case where the metal was in grid form. The mesh is of hybrid type (cubic and prismatic elements) and the number of elements and nodes were adjusted to achieve convergence of the results. For the calculations, we used 33991 elements and 10254 nodes respectively. The simulations are performed for lenses with concentration factor C_{geo} of 363×, i.e., the lens concentrates 363 times the direct normal irradiance on the solar cell. This value is chosen because it corresponds to the maximum concentration achievable with the lenses available in our laboratory for solar cells with an active

surface of 3×3 mm^2. The optical efficiency is η_{opt} is 0.92 and DNI on the lens is set to 900 W/m^2. The efficiency of solar cells η_{Cell} is set to 0.4 (i.e. 40% of the light received by the solar cell is converted into electricity and the rest is converted into heat). The heat to be dissipated $Q_{th,in,Pmpp}$ is calculated using equation (1). In this large-scale simulation, we assume that the glass used for the PCB and the Tedlar for the protection of the back surface of the bottom plate have the same emissivities as those employed in the CPV SMT prototype. The convection coefficients (Ain) and (Aout) are also assumed to be identical to those used in the previous simulation, as they have a negligible influence on the simulation results. The temperatures inside the module (T_{in}), ambient (T_{amb}), ground (T_{ground}), and lens (T_{lens}) are extracted from the literature [19]. The choice of reference [19] for these boundary conditions is motivated by our desire to simulate extreme conditions (higher temperatures) compared to our previously described experimental conditions. Additionally, these boundary conditions have been used in our previous work [12] to compare the performance of standard CPV modules using wire bonding with that of CPV SMT modules. The parametric simulation was conducted for two types of metal ribbons of different natures to compare thermal performances: copper ribbon and aluminum ribbon. Tables 3 and 4 provide the thermal properties and dimensions of the different materials used in this FEM and

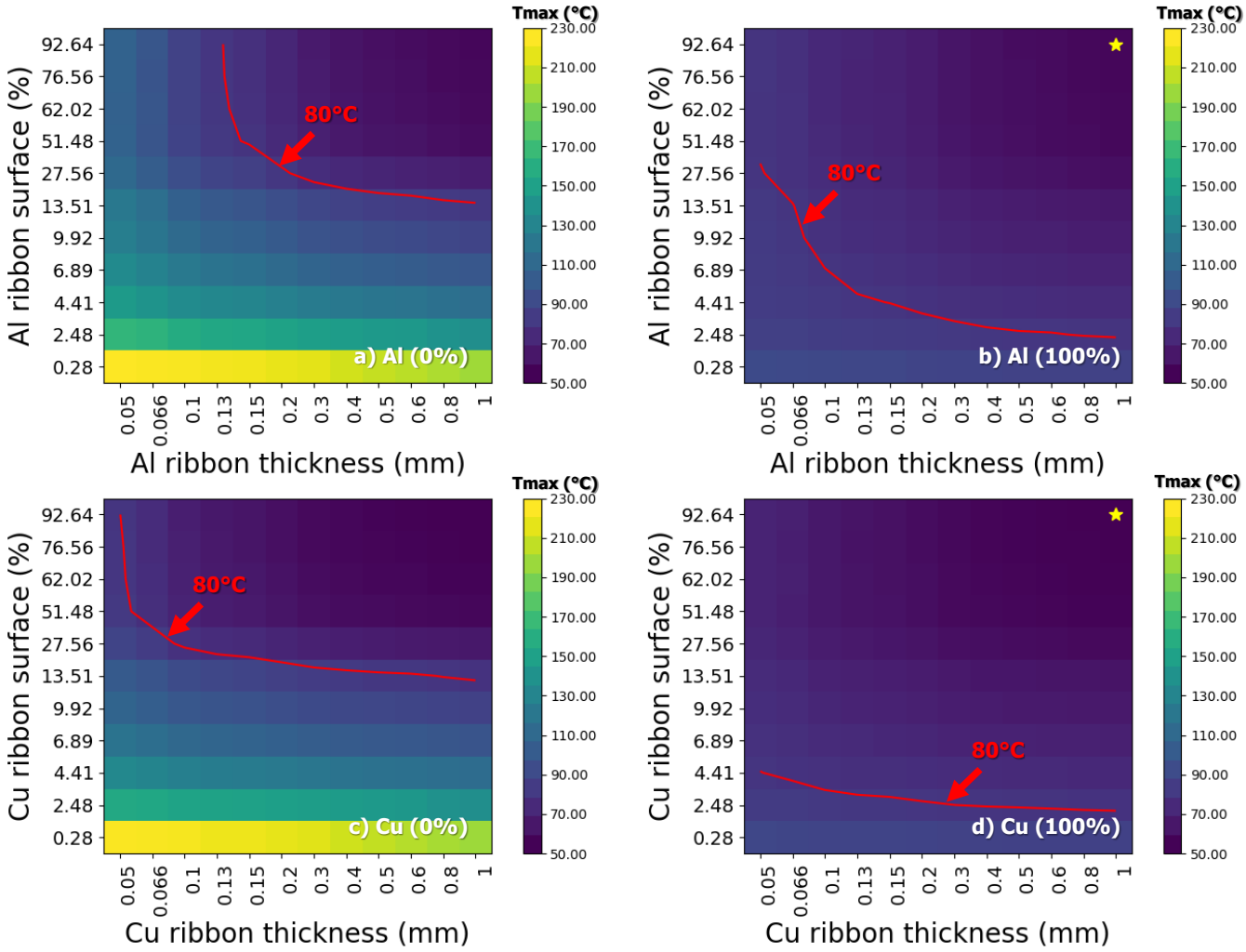

Fig. 8. Evolution of the maximum temperature of the solar cell as a function of the thickness and the surface of the Cu and Al ribbon. The simulations were performed for a metal coverage of the PCB of 0% and 100% i.e., 0 or 100% of the PCB surface is covered with metal except for the active area of the solar cell which is 9 mm^2. a) Al (0%), b) Al (100%), c) Cu (0%), d) Cu (100%). The red curves represent the 80°C levels for each simulation case. The yellow stars mark the simulation points corresponding to the lowest maximum temperatures for the solar cell.

the boundary conditions respectively [20, 32], and [19]. We then performed variations of the dimensions of the different parts of the basic package to evaluate the impact of the different parameters on the maximum cell temperature T_{max}.

2. Results and discussions

Several parameters and their dimensions were varied in the FEM model to evaluate their impact on solar cell temperature. We first varied the dimensions of the metal ribbon (Appendix 2-A and B) on the backside of the solar cell for two PCB metal coverage conditions 0% (Appendix 3-A and B) and 100% (Appendix 4-A and B). A 0% metal coverage means that the glass PCB is metal-free except for the contact pads. A 100% metal coverage means that it is entirely covered in metal, except for the active area of the cell. Metal ribbon thickness and area were varied, where area of the metal ribbon is expressed as a percentage, with an area of 57.143 × 57.143 mm^2 of metal ribbon corresponding to 100%. Additionally, two metal ribbon materials, copper, and aluminum, were compared. The EVA, Tedlar, glass and electrically conductive adhesive dimensions were fixed to (57.143 × 57.143 × 0.35 mm^3), (57.143 × 57.143 × 0.2 mm^3), (57.143 × 57.143 × 2 mm^3), and (3.4 × 3 × 0.05 mm^3) respectively.

Simulation results of the evolution of the maximum temperature of the solar cell as a function of the thickness and area of the metal ribbon behind the solar cell are shown in Appendix 9. The data in Appendix 9 was used to generate Fig. 8-a, b, c, and d. The red curves in each figure represent the combinations of ribbon thickness and area where the maximum temperature of the solar cell is equal to 80°C. Fig. 8-a (Al) and c (Cu) show the simulations result performed for a glass PCB with 0% metal coverage and fig 8-b (Al) and d (Cu) the simulations results performed for glass PCB with 100% metal coverage.

Figs. 8-a and b show that the maximum solar cell temperature decreases as the thickness and surface area of the aluminum ribbon increase for both PCB metal coverage rates. At 100% PCB metal coverage, the maximum cell temperature is lower than at 0% PCB metal coverage. The decrease in maximum temperature is more sensitive to the surface of the aluminum ribbon than to its thickness when the PCB metal coverage rate is equal to 100%. However, when the metal coverage ratio is 0%, to keep the maximum temperature of the solar cell below or equal to 80°C, the thickness of the aluminum ribbon must be greater than or equal to 130 µm, regardless of ribbon surface coverage. Under the most favorable dimensions considered here, ie a 92.64% metal ribbon surface area behind the solar cell, a ribbon thickness of 1 mm and 100% PCB metal coverage (corresponding to the yellow star in Fig. 6-b), the maximum solar cell temperature reaches 57°C.

Figs. 8-c and d shows similar trends when aluminum is replaced with copper, except that the decrease in maximum temperature is influenced more by the surface area of the copper ribbon than by its thickness for both cases of PCB metal coverage. Under the most favorable conditions, ie a 92.64% metal ribbon surface area behind the solar cell, a thickness of 1 mm and 100% PCB metal coverage (corresponding to the yellow star in Fig. 8-b), the solar cell temperature reaches 54°C.

The cell maximum temperature when PCB metal coverage is equal to 100% is lower than when PCB metal coverage is equal to 0% for both metallic ribbons (Al and Cu), which indicates that the presence of a metallic plane on the glass PCB enhances heat dissipation.

Regardless of the simulation scenario presented in Fig. 8, it is observed that the heat sink's surface has a more significant impact on reducing the maximum temperature than its thickness. This observation is explained by the fact that the thermal resistance of the heat sink is inversely proportional to its surface and proportional to its thickness, as indicated in Equation (3). Thus, a larger surface of the heat sink promotes better heat dissipation, while increased thickness diminishes this capacity. Nevertheless, in all simulation cases presented in Fig. 8, a decrease in the maximum temperature is observed as the thickness of the heat sink increases, reaching stabilization beyond a certain critical thickness. This result is in accordance with the literature [31]. This observation is explained by the fact that increased

thickness enhances the available surface for thermal conduction, allowing the heat sink to absorb more heat. Once the heat sink reaches a critical thickness, heat dissipation equals its generation, leading to temperature stabilization.

The red iso 80°C curves show that the dimensions required to keep the temperature of the solar cell below 80°C are larger for aluminum than for copper. This is due to the higher heat dissipation coefficient of copper over aluminum, which allows it to dissipate heat more effectively. The lower metal coverage of the PCB results in the need for large thickness-to-surface dimensions to maintain the solar cell temperature at 80°C. These results are consistent with those demonstrated in [12] and explain why the new module design dissipates heat better than the standard wire bonding assembly. Indeed, studies carried out in [12] showed that, under the same simulation conditions and with the same heat sink dimensions, the maximum solar cell temperatures were 58°C and 69°C respectively for the CPV module using SMT assembly with 100% metal coverage and the standard module using wire bonding. The improved heat dissipation of the new SMT modules makes it possible to design CPV modules with higher concentrations than those already available in the field.

The choice of the thickness-surface area dimension pair of the metal ribbon on the back of the solar cell and the metal coverage ratio of the PCB is crucial to limit the maximum temperature of the solar cell to 80°C or less. The optimal choice will depend on the type of application and must also consider concerns such as geometry, cost, and weight. The PCB metal coverage ratio will also be guided by the series resistance. Nevertheless, it should be noted that, due to the

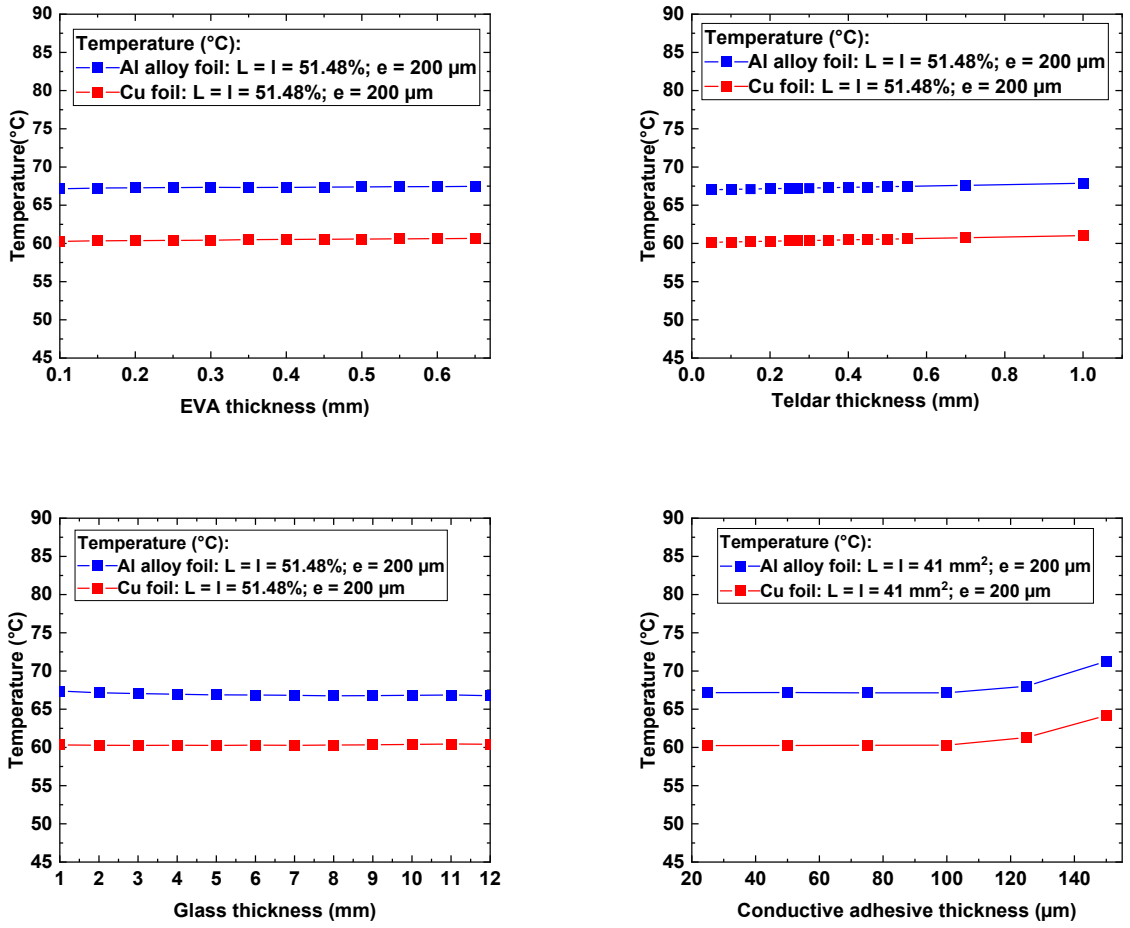

Fig. 9: Evolution of the maximum temperature as function the variation of thickness of EVA, Tedlar, glass, and conductive adhesive.

interconnections between the solar cells, neither the surface area of the metal ribbon behind the cell nor the metal covering the PCB can actually reach 100%.

We next evaluated the maximum temperature as a function of the thickness of various components of the module, namely the EVA, Tedlar, glass, and electrically conductive adhesive. The thicknesses were varied to match standard thicknesses available on the market: EVA from 100 µm to 650 µm (Appendix 5-A and B), Tedlar from 50 µm to 1 mm (Appendix 6-A and B), glass from 1 mm to 12 mm (Appendix 7-A and B), and electrically conductive adhesive from 25 µm to 150 µm (Appendix 8-B and B). The metal ribbon surface and thickness values were fixed at 51.48% and 200 µm respectively. Both Al and Cu metal ribbons were evaluated.

The results obtained are presented in Fig. 9. Within the thickness intervals studied for EVA and Tedlar, a negligible increase in maximum solar cell temperature, of around 0.4°C and 0.8°C respectively, was obtained irrespective of the type of metal ribbon (Cu or Al) used.

In the case of glass, over the thickness intervals examined, the maximum temperature of the solar cell decreased by around 0.6°C, irrespective of the type of metal ribbon (Cu or Al) used, and this variation is also considered negligible.

When the thickness of the electrically conductive adhesive varies from 25 to 100 µm, the maximum temperature of the solar cell increases by around 0.6°C, irrespective of the type of metal ribbon (Cu or Al) used, which is also negligible.

When the thickness of the electrically conductive adhesive increases further to 150 µm, the maximum temperature of the solar cell rises by around 3°C, again irrespective of the type of metal ribbon (Cu or Al) used. The temperature rise observed stems from the low thermal conductivity of the conductive adhesive. The increase in its thickness hinders the conduction and efficient dissipation of heat to the surroundings. While more significant than other aspects of this particular analysis, this variation is still considered as relatively low. Moreover, in practice, electrically conductive adhesives in CPV modules normally have a thickness of around 50 µm.

VI. Conclusion

Heat dissipation and resultant solar cell temperature was studied for a new Concentrator Photovoltaic (CPV) module design using a Surface Mount Technology (SMT) assembly method that was developed to simplify CPV module assembly. A 4-cell module was fabricated using this approach, whose properties and performance were used to feed a finite element simulation (FEM) model. The temperature distribution of the module, obtained by this numerical model, was in general agreement with experimental measurements of the module temperature made with an IR camera. However, temperature differences were observed at certain points in the module. These temperature variations between experiment and model are due to bubbles in the lamination and the presence of connecting wires. However, these problems can be improved by using a specialized laminator to avoid bubbles and by opting for a suitable PCB design and appropriate the presence of wires in the camera's field of view.

Parametric studies, using the FEM model extended to conditions of a large-scale CPV module, have determined that the dimensions of the metal ribbon at the back of the cell and the metal coverage ratio of the PCB are important parameters for thermal management of the CPV module. The other components (EVA, Tedlar, glass, and electrically conductive epoxy) of the module assembled with SMT do not have a significant impact on the module temperature. The temperature of the solar cell can be kept below 80°C over a wide range of dimensions of the metal ribbon behind the solar cell, both for a metal coverage of the PCB of 0% or 100%. However, this dimensional range is much wider when the metal coverage ratio is 100% than when the metal coverage ratio on the PCB is 0%. Under the best metal ribbon dimensions and PCB metal coverage ratio conditions, the temperature of the solar cell can be 54°C when the metal ribbon is copper, and 57°C when it is aluminum. These results demonstrate that in addition to simplifying the assembly process, using SMT for CPV modules fabrication can enhance heat dissipation both by the metallic layer on the glass PCB and on the back side contact. This opens the door to simpler CPV modules, higher performance CPV modules and higher concentration ratios.

VII. Acknowledgements

We acknowledge the support from STACE, NSERC and Prompt, for their material and financial support in the MARS-CPV project. LN2 is a joint International Research Laboratory (IRL 3463) funded and co-operated in Canada by Université de Sherbrooke (UdS) and in France by CNRS as well as ECL, INSA Lyon, and Université Grenoble Alpes (UGA).

Appendix 1: Thermal distribution on each solar cell, obtained from the finite element modeling of the CPV SMT prototype module.

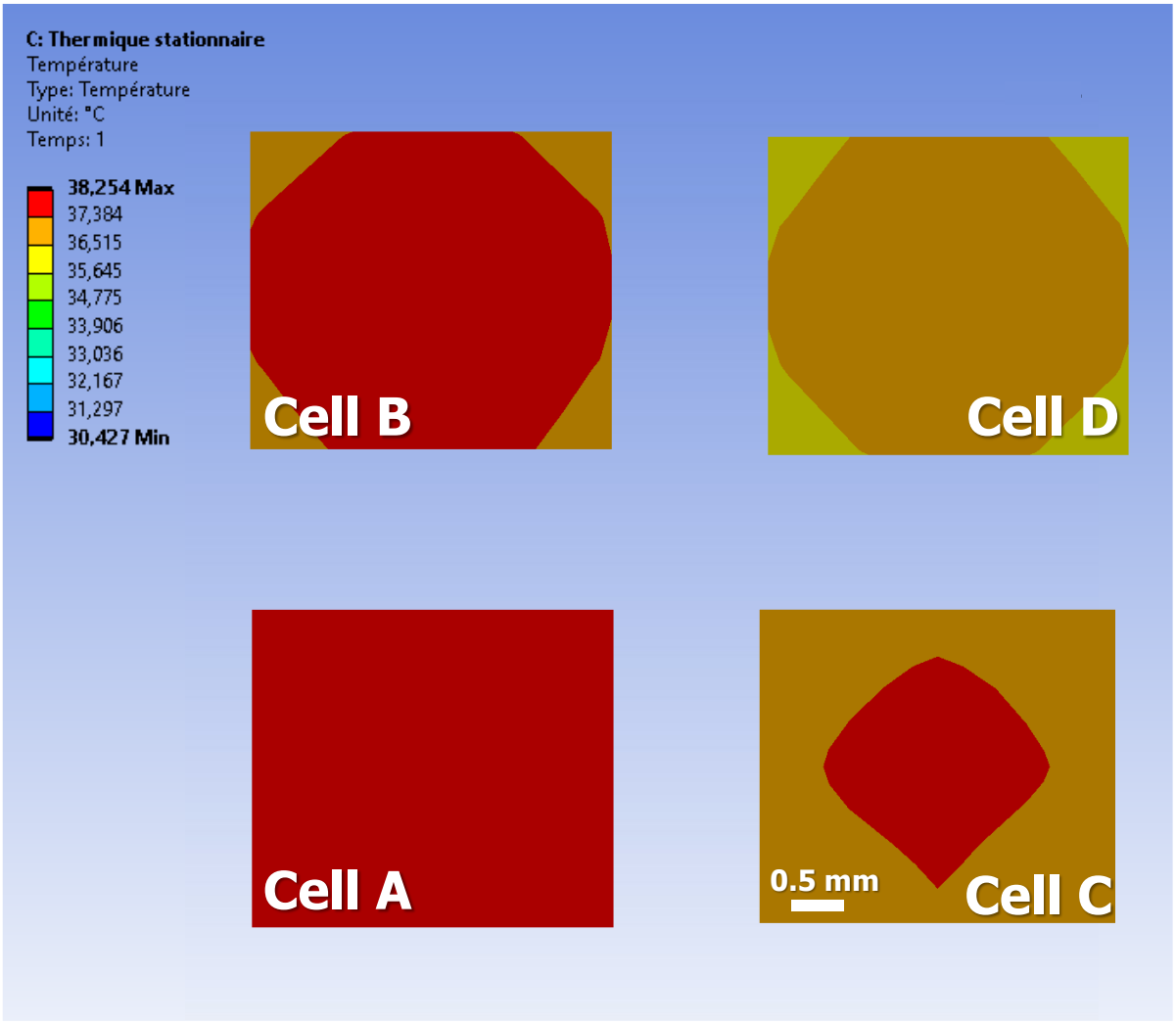

Appendix 2: Isometric view of the **rear face** of the infinite-scale model of the CPV module's bottom plate, showing: A) Variation in the metal ribbon surface, B) Variation in the metal ribbon thickness.

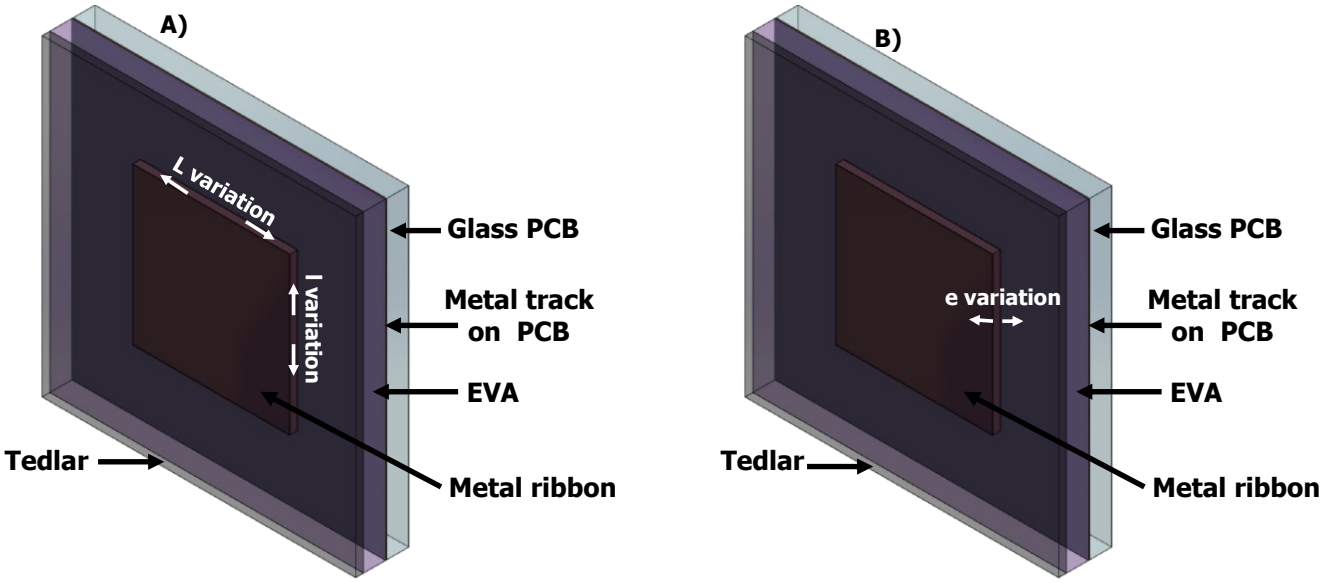

Appendix 3: A) Isometric view of the **front face** of the infinite-scale model of the CPV module's bottom plate with 0% metal coverage on PCB, B) Zoom of the corner of the bottom plate.

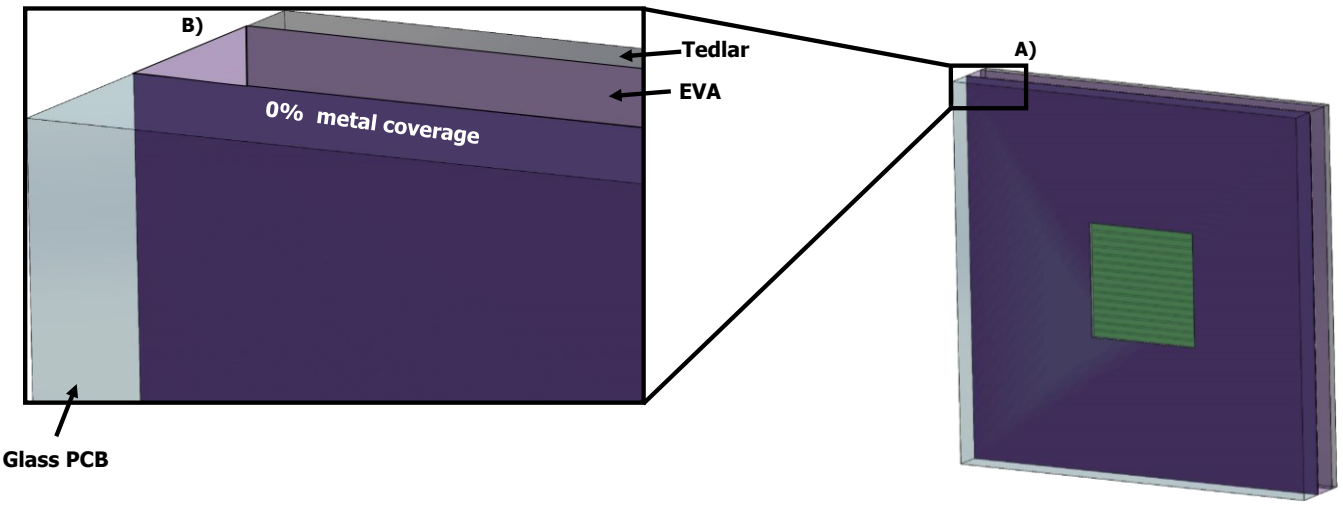

Appendix 4: A) Isometric view of the **front face** of the infinite-scale model of the CPV module's bottom plate with 100% metal coverage on PCB, B) Zoom of the corner of the bottom plate.

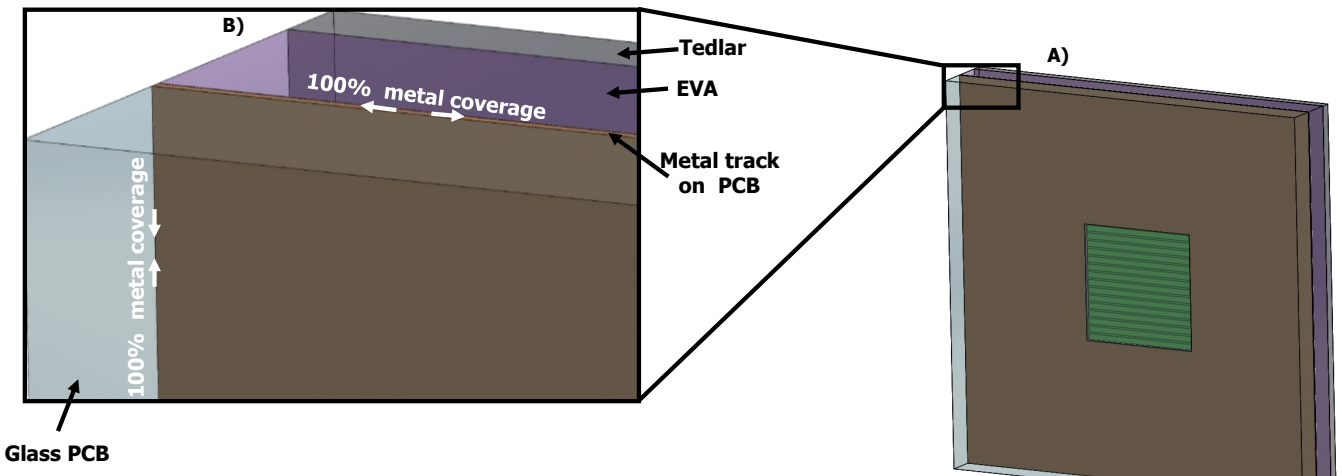

Appendix 5: A) Isometric view of the **front face** of the infinite-scale model of the CPV module's bottom plate with 100% metal coverage on PCB, B) Zoom of the corner of the bottom plate showing the EVA thickness variation.

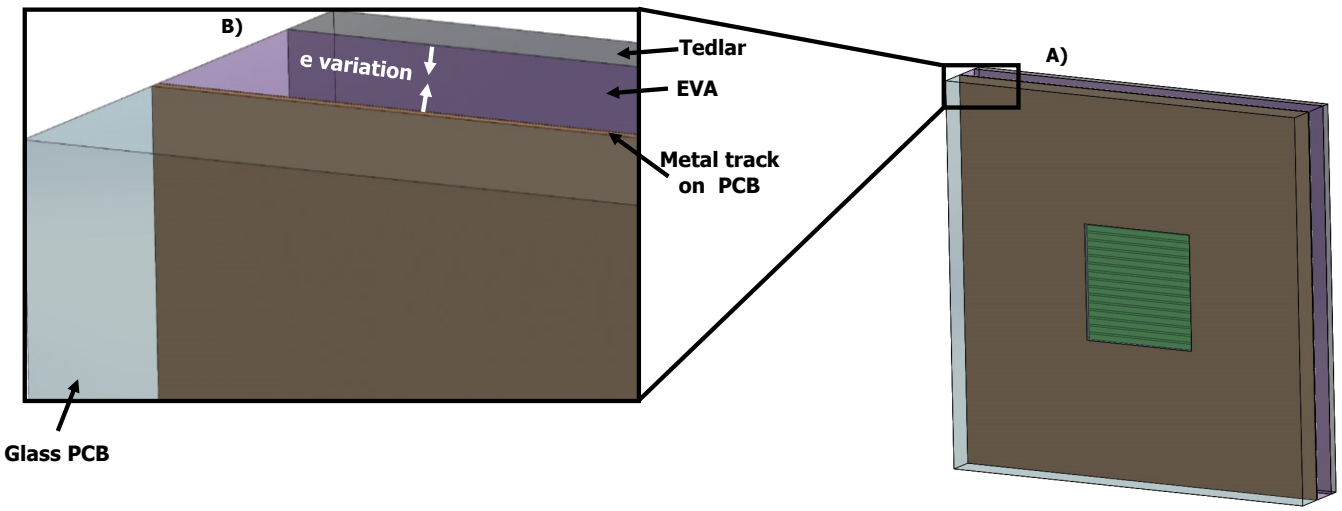

Appendix 6: A) Isometric view of the **front face** of the infinite-scale model of the CPV module's bottom plate with 100% metal coverage on PCB, B) Zoom of the corner of the bottom plate showing the Tedlar thickness variation.

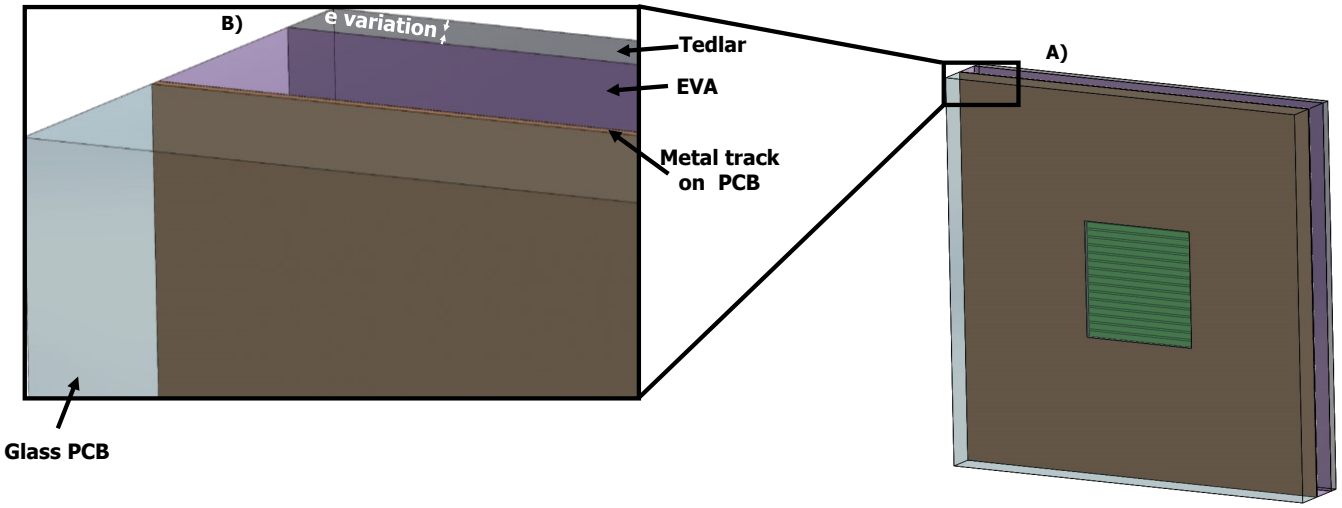

Appendix 7: A) Isometric view of the **front face** of the infinite-scale model of the CPV module's bottom plate with 100% metal coverage on PCB, B) Zoom of the corner of the bottom plate showing the glass thickness variation.

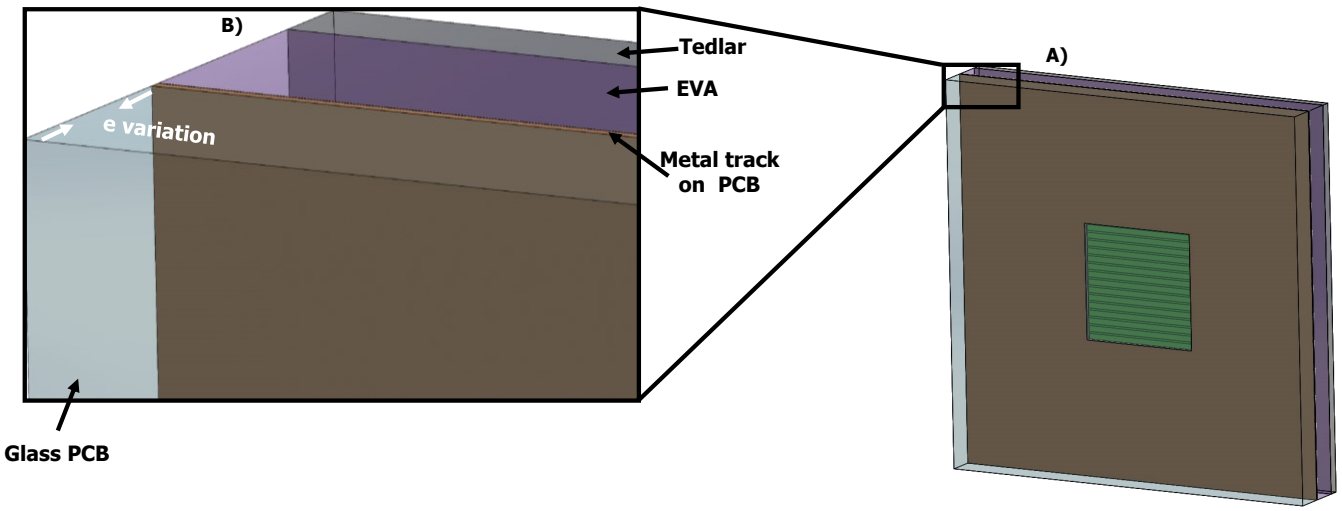

Appendix 8: A) Isometric view of the **rear face** of the infinite-scale model of the CPV module's bottom plate with 100% metal coverage on PCB, B) Zoom of the corner of the bottom plate showing the conductive adhesive thickness variation.

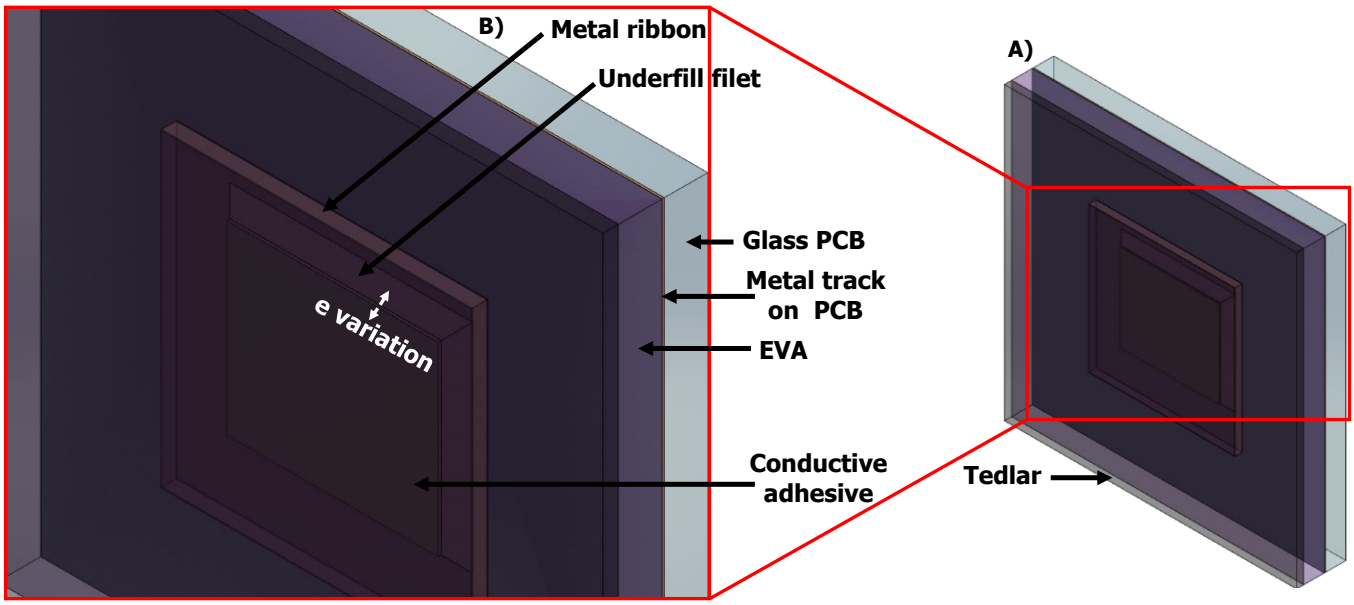

Appendix 9-A: Evolution of the maximum temperature of the solar cell as a function of the thickness and the surface of the al ribbon obtained by FEM. The metal coverage of the PCB was 0%. The values in orange represent the maximum temperatures obtained at each variation.

Thickness (mm) / Surface (%)	0.05	0.07	0.10	0.13	0.15	0.20	0.30	0.40	0.50	0.60	0.80	1.00
0.28	222.37	221.50	220.70	219.17	218.67	216.99	215.24	210.68	207.83	204.97	201.58	198.65
2.48	164.73	162.70	157.55	154.83	153.40	150.73	148.33	146.83	145.03	143.66	139.62	137.24
4.41	145.58	140.67	135.50	132.12	130.42	127.42	123.80	121.56	119.65	118.53	116.01	114.20
6.89	134.43	128.50	122.12	118.03	116.03	112.48	108.35	106.01	104.13	103.10	100.98	99.43
9.92	126.31	119.70	112.34	107.82	105.65	101.78	97.39	94.98	93.12	92.02	90.03	88.73
13.51	121.30	115.26	105.92	100.91	98.52	94.35	89.74	87.19	85.31	84.24	82.29	81.10
27.56	111.73	103.70	94.35	88.76	86.06	81.34	76.27	73.39	71.53	70.35	68.59	67.51
51.48	106.94	98.35	88.12	82.13	79.24	74.19	68.85	65.80	63.77	62.57	60.92	59.89
62.02	106.60	98.79	87.23	81.12	78.17	73.03	67.45	64.40	62.37	61.18	59.42	58.55
76.56	106.90	97.95	87.03	80.71	77.66	72.35	66.61	63.44	61.35	60.14	58.36	57.36
92.64	106.74	98.89	86.92	80.59	77.53	72.18	66.33	63.17	61.08	59.87	58.07	57.05

Appendix 9-B: Evolution of the maximum temperature of the solar cell as a function of the thickness and the surface of the al ribbon obtained by FEM. the metal coverage of the PCB was 100%. the values in orange represent the maximum temperatures obtained at each variation.

Thickness (mm) / Surface (%)	0.05	0.07	0.10	0.13	0.15	0.20	0.30	0.40	0.50	0.60	0.80	1.00
0.28	92.02	91.46	90.56	89.90	89.56	88.68	87.99	87.58	87.41	87.09	86.93	86.84
2.48	86.02	86.14	84.71	83.89	83.43	82.52	81.81	81.01	80.52	80.31	79.73	79.37
4.41	84.18	82.96	81.72	80.54	79.92	78.69	77.51	76.58	75.92	75.60	74.92	74.50
6.89	83.44	81.87	80.12	78.51	77.66	76.04	74.13	72.97	72.14	71.72	70.93	70.44
9.92	82.53	81.05	78.15	76.33	75.36	73.51	71.31	69.97	69.07	68.59	67.70	67.19
13.51	81.74	80.15	77.15	74.97	73.90	71.85	69.39	67.90	66.90	66.36	65.37	64.81
27.56	80.27	78.25	75.10	72.76	71.50	69.07	66.19	64.34	63.10	62.31	61.16	60.46
51.48	79.36	78.08	74.10	71.39	69.93	67.26	64.24	62.21	60.78	59.91	58.68	57.90
62.02	79.27	77.75	73.70	71.10	69.87	67.11	63.81	61.77	60.34	59.46	58.11	57.32
76.56	79.71	77.59	73.69	71.06	69.73	67.06	63.59	61.43	59.93	59.02	57.68	56.88
92.64	79.56	77.02	73.64	71.21	69.64	66.89	63.54	61.43	59.90	58.97	57.49	56.65

Appendix 9-C: Evolution of the maximum temperature of the solar cell as a function of the thickness and the surface of the copper ribbon obtained by FEM. the metal coverage of the PCB was 0%. the values in orange represent the maximum temperatures obtained at each variation.

Thickness (mm) / Surface (%)	0.05	0.07	0.10	0.13	0.15	0.20	0.30	0.40	0.50	0.60	0.80	1.00
0.28	221.06	220.59	219.82	218.29	217.84	216.18	214.57	209.90	206.98	203.94	200.66	197.87
2.48	155.73	154.43	151.83	150.86	150.29	149.27	147.40	146.13	144.48	143.18	139.41	137.08
4.41	132.86	129.77	126.66	124.72	123.73	122.01	119.84	118.40	117.04	116.30	114.96	113.47
6.89	118.38	114.87	111.16	108.90	107.80	105.85	103.57	102.24	101.03	100.30	98.74	97.52
9.92	108.29	104.22	100.01	97.56	96.42	94.38	92.08	90.81	89.74	89.09	87.70	86.75
13.51	101.36	97.54	92.24	89.56	88.30	86.18	83.86	82.61	81.60	81.02	79.73	78.93
27.56	88.67	83.69	78.31	75.35	73.98	71.63	69.20	67.82	67.03	66.44	65.54	64.95
51.48	81.89	76.53	70.63	67.48	66.02	63.55	61.04	59.65	58.74	58.21	57.54	57.06
62.02	80.86	76.03	69.41	66.18	64.69	62.16	59.55	58.17	57.27	56.74	55.93	55.65
76.56	80.63	74.95	68.60	65.27	63.73	61.14	58.47	57.07	56.17	55.65	54.84	54.42
92.64	80.06	75.24	68.36	65.01	63.45	60.84	58.13	56.72	55.82	55.30	54.49	54.06

Appendix 9-D: Evolution of the maximum temperature of the solar cell as a function of the thickness and the surface of the copper ribbon obtained by FEM. the metal coverage of the PCB was 0%. the values in orange represent the maximum temperatures obtained at each variation.

Thickness (mm) / Surface (%)	0.05	0.07	0.10	0.13	0.15	0.20	0.30	0.40	0.50	0.60	0.80	1.00
0.28	90.00	89.36	88.82	88.64	88.56	88.02	87.38	86.97	86.84	86.56	86.43	86.36
2.48	83.29	83.11	81.96	81.45	81.19	80.58	80.02	79.68	79.47	79.21	78.87	78.66
4.41	80.11	78.98	77.76	76.90	76.48	75.75	75.04	74.49	74.10	73.96	73.54	73.27
6.89	78.01	76.51	74.80	73.73	73.02	71.98	70.94	70.31	69.86	69.68	69.25	68.97
9.92	76.26	74.61	72.11	70.73	70.06	68.86	67.63	66.91	66.47	66.27	65.79	65.53
13.51	74.89	73.08	70.36	68.75	67.99	66.65	65.26	64.45	63.97	63.74	63.22	62.95
27.56	72.32	69.97	67.06	65.22	64.31	62.68	61.00	59.99	59.42	59.03	58.50	58.18
51.48	70.86	68.33	65.09	63.10	62.12	60.35	58.47	57.44	56.71	56.28	55.74	55.40
62.02	70.63	68.57	64.89	62.84	61.82	60.00	58.00	56.88	56.22	55.79	55.11	54.76
76.56	70.83	68.42	64.65	62.54	61.50	59.65	57.61	56.47	55.71	55.27	54.67	54.31
92.64	70.64	68.67	64.81	62.65	61.58	59.67	57.54	56.36	55.58	55.12	54.38	54.00

References

[1] M. A. Green *et al.*, « Solar cell efficiency tables (Version 61) », *Prog. Photovolt. Res. Appl.*, vol. 31, nº 1, p. 3-16, janv. 2023, doi: 10.1002/pip.3646.

[2] J. S. Foresi, R. Hoffman, D. King, et P. Ponsardin, « Performance of silicone-on-glass Fresnel lenses in EMCORE's Gen 3 high-concentration concentrator photovoltaic system », in *High and Low Concentrator Systems for Solar Electric Applications VII*, SPIE, oct. 2012, p. 84-89. doi: 10.1117/12.929348.

[3] M. Steiner *et al.*, « FLATCON® CPV module with 36.7% efficiency equipped with four-junction solar cells », *Prog. Photovolt. Res. Appl.*, vol. 23, nº 10, p. 1323-1329, 2015, doi: 10.1002/pip.2568.

[4] A. Luque et V. M. Andreev, Éd., *Concentrator photovoltaics*. in Springer series in optical sciences, no. v. 130. Berlin: Springer, 2007.

[5] M. Wiesenfarth, S. Gamisch, T. Dorsam, et A. W. Bett, « Challenges for thermal management and production technologies in concentrating photovoltaic (CPV) modules », in *Proceedings of the 5th Electronics System-integration Technology Conference (ESTC)*, Helsinki, Finland: IEEE, sept. 2014, p. 1-4. doi: 10.1109/ESTC.2014.6962842.

[6] M. Wiesenfarth, I. Anton, et A. W. Bett, « Challenges in the design of concentrator photovoltaic (CPV) modules to achieve highest efficiencies », *Appl. Phys. Rev.*, vol. 5, nº 4, p. 041601, déc. 2018, doi: 10.1063/1.5046752.

[7] T. Nakagawa *et al.*, « High-efficiency Thin and Compact Concentrator Photovoltaics with Micro-solar Cells Directly Attached to Lens Array », in *Light, Energy and the Environment*, Canberra: OSA, 2014, p. RF4B.5. doi: 10.1364/OSE.2014.RF4B.5.

[8] S. Burroughs *et al.*, « A New Approach For A Low Cost CPV Module Design Utilizing Micro-Transfer Printing Technology », présenté à 6TH INTERNATIONAL CONFERENCE ON CONCENTRATING PHOTOVOLTAIC SYSTEMS: CPV-6, Freiburg, (Germany), 2010, p. 163-166. doi: 10.1063/1.3509179.

[9] N. Hayashi *et al.*, « Thin concentrator photovoltaic module with micro-solar cells which are mounted by self-align method using surface tension of melted solder », présenté à 13TH INTERNATIONAL CONFERENCE ON CONCENTRATOR PHOTOVOLTAIC SYSTEMS (CPV-13), Ottawa, Canada, 2017, p. 080005. doi: 10.1063/1.5001443.

[10] J. H. Lau, « Cost analysis: solder bumped flip chip versus wire bonding », *IEEE Trans. Electron. Packag. Manuf.*, vol. 23, nº 1, p. 4-11, 2000.

[11] P. Elenius et L. Levine, « Comparing flip-chip and wire-bond interconnection technologies », *Chip Scale Rev.*, vol. 4, nº 6, p. 81-87, 2000.

[12] K. Kouame *et al.*, « New Triple-Junction Solar Cell Assembly Process for Concentrator Photovoltaic Applications », in *2023 IEEE 73rd Electronic Components and Technology Conference (ECTC)*, IEEE, 2023, p. 2223-2229.

[13] AZURSPACE, « Concentrator Triple Junction Solar Cell (0004357-00-01_3C44_AzurDesign_3x3.pdf) ». 4 janvier 2017. [En ligne]. Disponible sur: https://www.azurspace.com/images/products/0004357-00-01_3C44_AzurDesign_3x3.pdf

[14] SPECTROLAB, « CPV Point Focus Solar Cells, C4MJ Metamorphic Fourth Generation CPV Technology ». BOEING COMPANY, 16 juillet 2018. Consulté le: 21 août 2023. [En ligne]. Disponible sur: https://www.spectrolab.com/photovoltaics/C4MJ_40_Percent_Solar_Cell.pdf

[15] G. Segev, G. Mittelman, et A. Kribus, « Equivalent circuit models for triple-junction concentrator solar cells », *Sol. Energy Mater. Sol. Cells*, vol. 98, p. 57-65, mars 2012, doi: 10.1016/j.solmat.2011.10.013.

[16] P. Espinet-González *et al.*, « Temperature accelerated life test on commercial concentrator III-V triple-junction solar cells and reliability analysis as a function of the operating temperature: Temperature accelerated life test », *Prog. Photovolt. Res. Appl.*, vol. 23, nº 5, p. 559-569, mai 2015, doi: 10.1002/pip.2461.

[17] Loïc Mabille, « Vers la compréhension des mécanismes de dégradation et de vieillissement des assemblages photovoltaïques pour des applications sous haute concentration », PARIS-SUD, laboratoire des module photovoltaique CEA/Liten/DTS Institut National de l'Énergie Solaire (INES), 2014. [En ligne]. Disponible sur: https://theses.hal.science/tel-00985464/document

[18] T.-L. Chou, Z.-H. Shih, H.-F. Hong, C.-N. Han, et K.-N. Chiang, « Thermal performance assessment and validation of high-concentration photovoltaic solar cell module », *IEEE Trans. Compon. Packag. Manuf. Technol.*, vol. 2, nº 4, p. 578-586, 2012.

[19] M. Wiesenfarth *et al.*, « Technical boundaries of micro-CPV module components: How small is enough? », présenté à 17TH INTERNATIONAL CONFERENCE ON CONCENTRATOR PHOTOVOLTAIC SYSTEMS (CPV-17), Freiburg, Germany / Online, 2022, p. 030008. doi: 10.1063/5.0099878.

[20] J. F. Martínez, M. Steiner, M. Wiesenfarth, S. W. Glunz, et F. Dimroth, « Thermal analysis of passively cooled hybrid CPV module using Si cell as heat distributor », *IEEE J. Photovolt.*, vol. 9, nº 1, p. 160-166, 2018.

[21] L. Micheli, E. F. Fernández, F. Almonacid, T. K. Mallick, et G. P. Smestad, « Performance, limits and economic perspectives for passive cooling of High Concentrator Photovoltaics », *Sol. Energy Mater. Sol. Cells*, vol. 153, p. 164-178, 2016.

[22] C. Zhang, C. Shen, S. Wei, Y. Wang, G. Lv, et C. Sun, « A Review on Recent Development of Cooling Technologies for Photovoltaic Modules », *J. Therm. Sci.*, vol. 29, nº 6, p. 1410-1430, nov. 2020, doi: 10.1007/s11630-020-1350-y.

[23] A. J. Kinfack Leoga *et al.*, « Outdoor Characterization of Solar Cells With Microstructured Antireflective Coating in a Concentrator Photovoltaic Monomodule », *IEEE J. Photovolt.*, p. 1-4, 2023, doi: 10.1109/JPHOTOV.2023.3295498.

[24] IEC, « IEC 62670-3 INTERNATIONAL STANDARD ». IEC Webstore International Electrotechnical Commission, 7 février 2017. [En ligne]. Disponible sur: https://webstore.iec.ch/preview/info_iec62670-3%7Bed1.0%7Db.pdf

[25] J. Pern, « Module encapsulation materials, processing and testing. National Center for Photovoltaics (NCPV) », *Natl Renew Energy Lab*, 2008.

[26] K. Kouame *et al.*, « Indoor and Outdoor Characterization of III-V/Ge Solar Cells Assembled on Glass Substrate for Concentrated Photovoltaic Applications », in *2023 IEEE 50th Photovoltaic Specialists Conference (PVSC)*, San Juan, PR, USA: IEEE, juin 2023, p. 1-3. doi: 10.1109/PVSC48320.2023.10359819.

[27] S. Ahmed, Z. Li, M. S. Javed, et T. Ma, « A review on the integration of radiative cooling and solar energy harvesting », *Mater. Today Energy*, vol. 21, p. 100776, sept. 2021, doi: 10.1016/j.mtener.2021.100776.

[28] M. Xiao, L. Tang, X. Zhang, I. Y. F. Lun, et Y. Yuan, « A review on recent development of cooling technologies for concentrated photovoltaics (CPV) systems », *Energies*, vol. 11, nº 12, p. 3416, 2018.

[29] C. Algora et I. Rey-Stolle, Éd., *Handbook of Concentrator Photovoltaic Technology*, 1re éd. Wiley, 2016. doi: 10.1002/9781118755655.

[30] N. Jiang, A. G. Ebadi, K. H. Kishore, Q. A. Yousif, et M. Salmani, « Thermomechanical Reliability Assessment of Solder Joints in a Photovoltaic Module Operated in a Hot Climate », *IEEE Trans. Compon. Packag. Manuf. Technol.*, vol. 10, no 1, p. 160-167, janv. 2020, doi: 10.1109/TCPMT.2019.2933057.

[31] T.-L. Chou, Z.-H. Shih, H.-F. Hong, C.-N. Han, et K.-N. Chiang, « Investigation of the thermal performance of high-concentration photovoltaic solar cell package », in *2007 International Conference on Electronic Materials and Packaging*, IEEE, 2007, p. 1-6. Consulté le: 18 janvier 2024. [En ligne]. Disponible sur: https://ieeexplore.ieee.org/abstract/document/4510295/